NASA Contractor Report 4392

Three-Dimensional Compressible Turbulent Computations for a Diffusing S-Duct

C. F. Smith, J. E. Bruns,
G. J. Harloff, and J. R. DeBonis

CONTRACT NAS3-25266
APRIL 1992

NASA

NASA Contractor Report 4392

Three-Dimensional Compressible Turbulent Computations for a Diffusing S-Duct

C. F. Smith, J. E. Bruns,
G. J. Harloff, and J. R. DeBonis
Sverdrup Technology, Inc.
Lewis Research Center Group
Brook Park, Ohio

Prepared for
Lewis Research Center
under Contract NAS3-25266

National Aeronautics and
Space Administration

Office of Management

Scientific and Technical
Information Program

1992

Summary

The purpose of the present study was to evaluate the capability of the computational fluid dynamics computer program PARC3D to model flow in a typical diffusing subsonic S-duct, with strong secondary flows. This evaluation is needed to provide confidence in the analysis of aircraft inlets, which have similar geometries. The performance predictions include total-pressure profiles, static pressures, velocity profiles, boundary-layer data, and skin friction data. Flow in the S-duct is subsonic, and the boundary layers are assumed to be turbulent. The results, for both H- and O-grid solutions, are compared with existing test data. and interior flow measurements. The calculated and measured total pressures were also compared. Included in the discussion of the total-pressure contours is a description of the underlying physics of the development of secondary flows in turning ducts. Calculated and measured velocity vectors are shown to illustrate the development of the secondary vortices. A detailed discussion of the characteristics of the boundary layer is presented. The inviscid contributions to the secondary-flow field were quantified by solving the Euler equations for irrotational and rotational flow. Recommendations are made for further work in the modeling and testing of these ducts.

Introduction

Many aircraft induction systems include S-shaped subsonic diffusers with in- or out-of-plane bends. The cross-sectional geometries of these diffusers may include both rectangular and circular cross sections. Some examples include the Boeing 727, the Lockheed Tristar (L-1011), the General Dynamics F-16, and the McDonnell-Douglas F-18 aircraft. In the past much of the analysis of these inlets has been done by testing because the flow fields were too complex for numerical modeling. Most of this experimental work focused on low-speed or incompressible flows, although some data have been obtained for higher subsonic conditions. More recently, computational fluid dynamic studies have generally used parabolized Navier-Stokes (PNS) computer programs to predict the flows in these ducts. And considerable work has been done to model and test flows through S-shaped ducts. The literature review in the appendix summarizes these studies.

In contrast to these previously published studies, this study permits the inlet mass flow to adjust to the interior flow field conditions. The present study was conducted to evaluate the capabilities of a computational fluid dynamics computer program to model the flow physics and performance characteristics of a diffusing subsonic S-duct with moderate to high subsonic flow conditions. This was done by solving the full three-dimensional Navier-Stokes equations coupled with an algebraic turbulence model and by comparing the numerical results with test data. Solutions are obtained for an H- and O-grid in order to examine the effects of the type of grid on the solution.

Several aspects of the flow field were examined. The computed static-pressure field was compared with surface

Symbols

A	sublayer thickness
A^+	AU_t/ν
C_f	skin friction coefficient
C_{ps}	static-pressure coefficient, $(P_s - P_{s,\mathrm{ref}})/Q_{\mathrm{ref}}$
C_{pt}	total-pressure coefficient, $(P_t - P_{s,\mathrm{ref}})/Q_{\mathrm{ref}}$
D	upstream duct diameter
P_s	static pressure
P_t	total pressure
Q	dynamic pressure
Re	Reynolds number, $\rho_{\mathrm{ref}}\,\mu_{\mathrm{ref}}\,D/\mu$
S	centerline duct arc length
T_w	wall shear stress
U^+	flow velocity normalized by friction velocity
U_t	friction velocity, $\sqrt{(\lvert T_w\rvert/\rho_w)}$
u	velocity in x direction
v	velocity in y direction
w	velocity in z direction
x	coordinate distance (see fig. 1)
$Y+$	normalized distance in wall coordinates, yU_t/ν
y	coordinate distance (see fig. 1)
z	coordinate distance (see fig. 1)

δ boundary-layer thickness

μ viscosity

ν kinematic viscosity

ρ density

ϕ circumferential angular position around duct

Subscripts:

ref reference station (station I)

Description of Test Data

The experiment of Vakili et al. (ref. 1) is modeled. The duct had a circular cross section with two 30° bends (see fig. 1). The area ratio of the duct exit to inlet is 1.51, and its variation as a function of axial distance is also shown in figure 1. A 30-in. section of straight pipe was connected to the exit of a wind tunnel to provide the flow and turbulent boundary layers entering the S-duct. The inlet boundary layer was turbulent and was about 7.8 percent of the 3.25 in. upstream duct inside radius. The average inlet Mach number was 0.6. The radius of curvature was 32.5 in., which is approximately 5 inlet duct diameters. A 60-in. straight section of pipe, installed behind the S-duct, conducted the flow to the exit (ambient air). The Reynolds number was 3.25×10^6 per foot. The offset of the S-duct is approximately 1.5 upstream duct diameters.

Vakili et al. measured wall static pressures along three azimuth angles of 10°, 90°, and 170°. (The azimuth angles were offset 10° from the planes of symmetry (0°,180°) to avoid structural joints.) Total- and static-pressure profiles were measured at six axial measurement stations (fig. 1(b)). The data were compared with our computed results. In addition, velocity vectors derived from the data were compared with those obtained from the numerical model.

Numerical Modeling

In this section, several aspects of the numerical modeling of the flow through the diffusing S-duct are discussed. The flow analysis code is briefly presented. Following this, a discussion of the grid generation process and the boundary conditions used are presented.

Computer Program

The PARC3D computer program (ref. 2) was used to predict the flow within the diffusing S-duct. This code solves the full three-dimensional Reynolds-averaged Navier-Stokes equations in strong conservation form with the Beam and Warming approximate factorization algorithm. The implicit scheme uses central differencing for a curvilinear set of coordinates. The code was originally developed as AIR3D by Pulliam and Steger (ref. 3). Pulliam later added the Jameson artificial dissipation (ref. 4) and called the code ARC3D (ref. 5). Cooper adapted the ARC3D code for internal propulsion application and named the code PARC3D. The Baldwin-Lomax algebraic turbulence model (ref. 6) was used.

Grid

The cross-sectional shape of an aircraft inlet often changes from rectangular at the inflow station to circular at the compressor face. One type of grid, then, does not conform well to the boundaries throughout the duct. An H-grid conforms well to a rectangular shape, and an O-grid to a circular one. In this study the effects on the numerical solutions using an H-grid and O-grid to model a circular, diffusing S-duct were investigated to determine the numerical differences. The major problem with the O-grid is the so-called "pole" boundary condition, which is applied at the center of the grid. This boundary condition averages the results along the adjacent grid line and applies this average to all the points along the inner most line. On the other hand, the major problem with the H-grid is that it does not conform well to a curved boundary. In particular, the "corner points" of the grid exhibit excessive skewing.

The H-grid of this study (fig. 2) has 75 points in the streamwise direction and 33 by 33 points in the cross-stream directions. The O-grid (fig. 3) has 65, 49, and 26 points in the streamwise, circumferential, and radial directions, respectively. The upstream and downstream lengths of straight duct are the same for both grids. The O-grid was generated using an algebraic grid generation technique. The upstream and downstream ducts were extended using hyperbolic stretching functions. The H-grid was generated using the INGRID3D code (ref. 7). The diffusing S-duct H-grid was generated by expanding the similar nondiffusing S-duct H-grid at each streamwise station to match the local cross-sectional area for the diffusing S-duct. An algebraic approach was used to obtain the initial grid for the nondiffusing S-duct. This grid was then smoothed using an elliptic equation solver.

Boundary Conditions

The boundary conditions used were no slip on the walls; total pressure and temperature conditions specified at the entry plane, using experimental values obtained at the reference station (station I); and static pressure specified at the exit plane. A pole boundary condition was used for the center of the O-grid. The implementation of these boundary conditions for each grid is illustrated in figure 4.

Results

In this section, the numerical results for static pressure, total pressure, and velocity vectors are compared with measured data. In addition, details of the boundary layers are discussed that include boundary-layer development through the duct, velocity profiles in wall coordinates, and the prediction of flow separation. Numerical aspects of the solutions are also discussed.

Static Pressure

The surface static-pressure distributions obtained from the H- and O-grid solutions are compared with the measured distribution in figure 5. The experimentally and numerically determined separation and reattachment points are indicated in the figure. The separation region was determined by the change in sign of the streamwise velocity component nearest to the wall. The H-grid solution provides better agreement with the data downstream of the separation than does the O-grid solution. (This result appears to be fortuitous for reasons that will be discussed in a later section concerning the calculated turbulent viscosities.) The difference between these two solutions may be attributable to the poor prediction of flow separation. In fact, surface static pressures calculated in a nondiffusing, nonseparating S-duct (ref. 8) were in good agreement with the data, which lends further support to the premise that the poor prediction of separation contributes to the discrepancies between the measured and calculated static pressures in the separating duct flow. Another possible cause for the disagreement with the data is the difference between hardware and analytical surface smoothness. The ±1/8-in. tolerance of the test hardware surface definition resulted in a wavy surface, which could be detected by visual inspection. That wavy surface could account for some of the discrepancy between the data and the numerical results for a smooth analytical surface.

Comparisons of the experimental static-pressure contours and those obtained using the O- and H-grids are shown in figure 6. Some differences between the O-grid and H-grid solutions are present. Through the first bend, (figs. 6(a) to (c)), the static-pressure contours calculated by the H- and O-grids are similar. In the second bend (figs. 6(d) to (e)), the contour levels calculated using the two grids are very different. The levels obtained using the H-grid are much lower than those obtained with the O-grid because the height above the surface of the calculated separation bubble is greater for the H-grid than for the O-grid. This larger bubble causes the flow to move at a higher velocity around it and thus results in a lower static-pressure field. This lower static pressure is also indicated in the surface static-pressure distributions of figure 5.

The calculated contours do not agree well with the data. The static-pressure gradients near the duct wall are not present in the calculated pressure contours. This may be due to the extrapolation of the static pressure from the first grid point off the wall, which is equivalent to specifying a zero static-pressure gradient. Other contributing factors may be the that turbulence model does not handle the secondary-flow field adequately or that the grid does not adequately resolve the secondary flow field.

Total Pressures

Total-pressure contours are compared in figure 7. Agreement is reasonable between the H- and O-grid solutions. The pole boundary in the center of the flow field with the O-grid tends to create distortions in the flow field near this boundary (fig. 7(f)). The agreement between the numerical results and the data is not as good at the duct exit (station VI) as at the first bend (station IV). The secondary flow develops very rapidly in the second bend (Compare the total-pressure contours at stations III and IV with stations V and VI.) This rapid development may be attributed to the change in the static-pressure gradient, which, in the second bend, tends to reinforce the secondary-flow development. In the first bend (fig. 6(b)) the region of high pressure is along the outer wall (concave side) of the duct, which tends to retard fluid motion from the inner wall (convex side). In the second bend (fig. 6(d)) the higher static pressure is along the inner wall of the duct, which is now concave, and tends to "push" the flow away from this wall. In addition, because of the diffusive nature of the duct, a large adverse pressure gradient causes the flow to separate in the streamwise direction. The computed total pressures at station VI (fig. 7(f)) indicate that the secondary flow is not as strong as the experimental flow, because the calculated region of "inviscid" core flow is larger than the measured region. The region of core flow lies within the 1.05 total prerssure contour. This discrepancy, in secondary flow strength, may be due to boundary-layer resolution and/or turbulence modeling. The Y^+ distance of the first grid point off the wall is approximately 10, which is in the buffer layer. Further grid refinement in the crossflow directions may improve the resolution of the vortical flows. The theoretical maximum total-pressure coefficient is 1.1, as compared with the experimental maximum of 1.05 as shown in the figures.

Velocity Vectors

The scaled velocity vectors computed with the O- and H-grids are compared with the data of figure 8. The velocity vectors in the H-grid solution indicate the presence of noise in the solution near the corners of the computational grid. This noise is attributed to the very large amounts of grid skewness in these corner regions. The overall solution does not appear to be affected by this skewness. The O-grid velocity vectors do not indicate a similar problem.

The results and data are in reasonable agreement. The computed results indicate that the magnitude of the velocity vectors is smaller than that in the data, which is consistent with the observation of underprediction of secondary flow made in regards to the total-pressure contours. The center of

the vortex moves closer to the plane of symmetry and away from the wall as the flow progresses through the duct. This is observed in the computed and experimental velocity vectors.

Through the first bend (figs. 8(a) to (c)) the velocity vectors indicate very little secondary-flow development. In the second bend (figs. 8(d) to (e)) the vortices become very pronounced. This is consistent with the discussion concerning the total-pressure contours.

Boundary Layers

The variation in boundary-layer thickness at $\phi = 0$, 90°, and 180° as a function of duct length is shown in figure 9. The boundary-layer thickness was defined as the normal distance from the surface where the total-pressure coefficient was 99 percent of the free-stream value. These predictions were obtained from the O-grid solution and are compared with the data. The corresponding growth of a boundary layer along a flat plate is also shown for comparison. The most significant departure from the growth along a flat plate is for $\phi = 180°$, which contains the separated region and the secondary-flow vortices. The data indicate a more rapid boundary-layer growth near the duct exit ($S/D = 5$) than the computations indicate. This is consistent with the previous finding that the computations underpredict the secondary-flow development. The measured boundary-layer growth follows the growth along the flat plate at the other two locations. The calculated growths deviate from this trend.

The velocity profile, in wall coordinates, is shown in figure 10 for stations I, IV, and VI for the O-grid. Since the first grid point was outside the linear region (viscous sublayer, $Y^+ < 7$), an accurate value for the friction velocity could not be obtained by direct differentiation. Instead, the friction velocity was used as a variable to normalize the computational results by a successive substitution procedure that forced one of the points to fit the law of the wall for a flat plate. The viscous sublayer region, the log linear region, and the wake regions are indicated in the figure. At the reference station the calculated boundary layer agrees very well with the log-linear region. Because at station IV the flow is separated (fig. 5) and because the definition of the friction velocity is not applicable, the velocity profile is not shown for this station at $\phi = 170°$. At station VI the flow is reattached (fig. 5), and a large vortical flow is present (fig. 8(e)), which causes the boundary-layer profile to deviate from the law of the wall for $\phi = 170°$. A comparison of the calculated and measured velocity profiles for station VI is shown in figure 10(d). The data, which were available for this station only, were normalized using the same procedure as was used for the computed results. Although the quantitative agreement is poor, the trends are similar. Some of the discrepancy may be attributable to the lowest Y^+ for the data being approximately 800, which may place the data in the wake region where the flow is not log-linear. The assumption in the normalization procedure is that the first point lies within the log-linear region.

The skin friction coefficients, obtained from the O-grid solution, are plotted as functions of axial distance for $\phi =$ 10°, 90°, and 170° in figure 11. The calculated trends are similar to the trends exhibited by the data (ref. 9) for low-speed flow in a nondiffusing S-duct. This comparison provides another check on the trends observed in the computed results. Note that C_f values for the experiment do not exist. The shear velocities for the O-grid and data are shown in table I. Discrepancies between the data and the computed results may be due to the fact that the first data point is so far from the wall ($Y^+ = 800$).

The coefficient A^+ in the Baldwin-Lomax turbulence model was varied depending on the streamwise pressure gradient as given in reference 10. Previous studies have indicated that adjusting A^+ in this manner can improve the prediction of separated flows. Although the variations in A^+ were large, no significant improvements obtained over a constant A^+.

Turbulent Viscosity Calculations

Contours of turbulent viscosity are shown in figure 12 at the reference station for the H- and O-grids, which is upstream of the S-duct's first bend. The H-grid contours are not smooth or concentric, because of the presence of multiple walls and of the use of the minimum turbulent viscosity calculated at a point due to each wall. The O-grid turbulent viscosities are symmetric since only one "wall" is present.

TABLE I. - FRICTION VELOCITY USED TO NORMALIZE VELOCITY AND C_f, O-GRID

Station	Axial position, deg	Friction velocity, U_t, ft/sec	Edge velocity, U_e, ft/sec	Velocity ratio, U_t/U_e
O-grid calculation				
I	10	24.78	740	0.0335
	90	24.79	740	.0335
	170	24.81	740	.0335
IV	10	20.05	586	0.0342
	90	18.28	586	.0312
	170	4.34	586	.0074
VI	10	15.15	485	0.0312
	90	16.41	485	.0338
	170	13.49	485	.0278
Experiment				
VI	0	17.45	434	0.0402
	100	19.48	439	.0444
	180	12.86	288	.0446

The H-grid turbulent viscosities decrease very rapidly near the plane of symmetry; whereas the O-grid contours show sustained levels in this region. This difference may account for the differences observed in the calculated static-pressure distributions obtained by using the two grids.

To investigate this point, a sensitivity study was performed in which the O-grid's calculated turbulent viscosities were reduced by a factor of 3. The selection of this factor was based on the comparisons of measured and calculated shear stresses reported in reference 11. The calculated static-pressure distributions are shown in figure 13. As can be seen, the calculated static pressures compare much more favorably with the data using the reduced turbulent viscosities (c.f. fig. 5(a)): The calculated point of separation is closer to the experimentally observed separation point. But the reattachment point, which is associated with the lower turbulent viscosity, is farther downstream of the experimental point. This sensitivity study indicates that the current algebraic turbulence model may be predicting turbulent viscosities that are too large.

Another aspect of turbulence modeling is the determination of the length scale. The Baldwin-Lomax model implemented in the PARC3D code searches the entire computational domain for this scale. The turbulent viscosities obtained with the O- and H-grids at stations IV and VI are shown in figures 12(b) and (c). At station IV high turbulent viscosities are confined to regions near the wall. However, at station VI, where the vortex is much more developed, high turbulent viscosities occur in the core region of the duct where lower values should be found. Up to the first bend (station IV) the vortex development is minimal, and the flow exhibits as a typical boundary layer, which the turbulence model handles fairly well. In the second bend, the high turbulence in the core region of the duct may result from the turbulence model improperly using the vortical flow region as part of its length scaling region. This situation may be improved by restricting the range of the search to a region close to the duct wall. Additional length scales may be needed to model the free shear layer of the vortex. However, measurements of turbulence quantities are needed to validate this approach.

Flow Separation

The calculated particle trajectories in the flow separation region are compared with the paint flow visualization in figure 14. The calculated flow field is in general agreement with the data. However, the calculated location of the separation, for both grids, is approximately one-half of a duct diameter downstream of the actual point of separation. Improved grid resolution in this region of flow separation may improve the computed results. In addition, the inaccurate prediction of the separation may be partially attributed to the simple turbulence model used. The Baldwin-Lomax turbulence model is valid for two-dimensional, separating flows. In this case the flow is three-dimensional with a very strong secondary flow. This case may be beyond the capabilities of the Baldwin-Lomax turbulence model. The large hardware tolerances for the test model may also have contributed to the poor agreement.

The discrepancies in the two solutions may be due to the lower turbulent viscosities calculated for the H-grid solutions near the plane of symmetry (fig. 12) than those used in the O-grid calculations. The separated flow lies along this plane of symmetry; thus, the calculated recirculation region could be affected by the level of turbulent viscosity present.

Numerical Issues

The residuals for these numerical solutions were reduced approximately three orders of magnitude. The mass flow changes between the inlet and exit are within 1 percent for all the calculations. The number of iterations required to obtain a converged solution was approximately 30 000. Solutions were obtained on the Cray-XMP and Cray-YMP. The computational speed for the H-grid solutions was 800 iterations per CPU hour, and for the O-grid solutions 1000 iterations per CPU hour using the Cray-XMP. The speeds obtained are different because the H-grid requires two sweeps in the turbulence model, because of the two walls, and the O-grid requires only one sweep. The computational speed obtained using the faster Cray-YMP was by approximately a factor of two greater.

Inviscid Contributions

To investigate the inviscid contributions to the secondary flow, the Euler equations were solved for irrotational and rotational inflow conditions using an O-grid. For both flow cases, the downstream pressure was adjusted to obtain the fully turbulent calculated mass flow at the upstream boundary. An incoming uniform flow was used for the irrotational flow case; for the rotational flow case, the calculated conditions at the duct upstream reference station were held fixed, and the downstream flow was considered inviscid. The upstream velocity profile used for the rotational flow case is shown in figure 15. As shown in this figure, the computed velocity profile is very close to the 1/7th power law profile.

Figure 16 shows the computed surface static pressures for the irrotational and rotational flow cases. The general shapes of these profiles are similar to each other and to the data. The similarity implies that the streamwise pressure gradients are determined primarily by potential effects. The experimental pressure levels are influenced by the rotational and viscous effects, of course. The streamwise pressure gradient used in a PNS code is generally derived from either a potential or an inviscid, rotational flow solution.

Classical theories (ref. 12) concerning secondary flow in ducts attribute their origins to the streamwise turning or deflection of the transverse vorticity component generated in the incoming boundary layer. This vortex stretching results

in the generation of counterrotating vortices. The irrotational flow results showed no secondary-flow development, which gives confidence in the calculations. Figure 17 shows the total-pressure contours at various stations throughout the duct for inviscid, rotational flow. And figure 18 shows the associated secondary-flow velocity vectors. In these figures, the rotational results are compared with the calculated turbulent flow results. As can be seen, much of the secondary flow observed in the experimental results can be attributed to the vorticity in the upstream boundary layer. Therefore, accurate prediction of the boundary layer is very important in the calculation of secondary flows in S-ducts. To accomplish this, an adequate number of grid points should be provided to resolve the boundary layer properly. The streamwise pressure gradient is primarily a potential flow phenomena, and a significant portion of the secondary flow can be obtained by solving the rotational, Euler equations with an accurate upstream initial plane of data or computed results. With a PNS solver the upstream inflow boundary is usually provided from data or an FNS solution. Contours of streamwise vorticity are shown in figure 19(a) for inviscid, rotational flow and in figure 19(b) for fully turbulent flow. In particular, there is a rapid increase in the amount of streamwise vorticity present when comparing stations V and VI with stations III and IV. This is due to the increase in size of the secondary-flow vortices. As can be seen in the figures, the inviscid, rotational flow accounts for a significant portion of the secondary flow. The magnitudes of the vorticity contours for the inviscid, rotational flow field are larger than those obtained from the viscous flow field. A similar phenomena is noted in reference 13, whose authors attribute this to the turbulence model actually dissipating the strength of the secondary-flow field. This is consistent with the previous discussion of the current turbulence model providing turbulent viscosity levels that are too high.

This discussion of the inviscid contributions to the secondary-flow development in S-ducts highlights the need to accurately define the upstream boundary conditions for an aircraft inlet. Without proper upstream boundary conditions, the computed flow field at the inlet exit will not be accurate. With an actual aircraft, the incoming flow may contain vortices that were shed from upstream components. Therefore, detailed measurements must be made at the inlet entrance to provide adequate upstream inlet boundary conditions for FNS or PNS solvers. The alternative is to obtain an upstream FNS solution accounting for the appropriate airframe components. These results also indicate that inviscid, rotational flow solutions may be useful in preliminary screening of S-duct designs.

Concluding Remarks

The overall solutions obtained using the O-grid and the H-grid were similar, although differences were present in the details. The O-grid provided a solution that had no noise in the velocity field and a consistent level of turbulence near the plane of symmetry. This is attributable to the presence of one wall when an O-grid is used. The use of multiple walls with the H-grid introduces these distortions. The pole in the center of the O-grid produced a local distortion in the flow field when flow gradients were present in this region. These distortions did not significantly influence the overall results.

The upstream and downstream boundary conditions for the duct should be accurately specified to allow for the proper upstream boundary-layer development and downstream pressure adjustment. One check on the validity of the solution is to plot the upstream boundary layer in wall coordinates (U^+ versus Y^+). The calculated velocity profile should follow the universal law of the wall in regions where the flow is unseparated. The mass flow changes between the inlet and the exit of the S-duct should be within 1 percent as one of the criteria for a converged solution.

The computed total pressures and velocity vectors are generally in good agreement with the data. However, the calculated static pressures are not—probably because of the poor prediction of separation. Therefore, the results obtained for separating flows must be cautiously interpreted. Two counterrotating vortices at the S-duct exit were calculated, which is consistent with the flow physics. The rotational Euler solutions show that the development of the secondary flows in S-ducts is driven by inviscid phenomena, provided viscous flow is ingested.

Finer grid resolution may improve the results significantly. Vortical flows may require many more grid points in the crossplane than have been used. In addition, the region of flow separation requires more grid points in the streamwise direction. Adaptive gridding schemes may also provide for better resolution of flow gradients by packing the computational grid in these regions. To resolve the boundary layer properly, it is important to have the first grid point off the wall in the Y^+ region of less than 10 in order to place a calculation point in the viscous sublayer.

The computation may be improved by incorporating a two-equation turbulence model, such as the k-e turbulence model, in order to improve the prediction of the secondary flows. In many such models wall functions are used. These may not be adequate to model the effects of the secondary flows. If this is the case, near-wall or low-Reynolds-number k-e models may have to be used, and such models would increase computational time even more than would the use of the wall functions. If the two equation models are not adequate, the use of higher order turbulence models such as the Reynolds stress equations may be necessary.

More compressible data, that is, detailed flow measurements, are needed to validate the turbulence models. These measurements would include turbulent stresses and velocities. The data could then be compared with the numerical predictions in order to fully evaluate the ability of a turbulence model to predict the proper flow physics in terms

of the Reynolds stresses and universal velocity profiles. Measured skin friction would provide another source of data for verifying the turbulence models used. The diffusing S-duct discussed in this paper should be rebuilt and tested to take advantage of improved experimental techniques that have been developed during the past several years. By testing this duct, the numerical results for comparison are already available and could be used to guide the test program in terms of data requirements.

Tests that address some of the issues dealing with inlets at angles of attack should also be performed. Test and calculations could be made to study the effects on the internal flow in S-ducts at low angles of attack where the flow is attached to the inlet lip. Also, studies of inlets at high angles of attack for the case where the flow is separated along the inlet lip would be very useful.

Appendix—Literature Review

Experiments

Bansod and Bradshaw (ref. 9) conducted experiments using three constant area S-ducts. The flow was incompressible with a Reynolds number of 0.5×10^6 based on diameter. The streamwise deflection of the boundary layer in the first bend produced streamwise vorticity and a pair of vortices formed at the outside (radius) of the second bend and caused the boundary-layer thickness to increase rapidly. Willmer et al. (ref. 14) tested a circular inlet and an S-duct at Mach numbers from 0 to 0.21 and at incidence and sideslip angles from 0 to 40°. Losses at the engine face were determined as a function of lip shape, contraction area ratio, boundary-layer transition location, lip slot, and offset diffuser. Guo and Seddon (ref. 15) experimentally investigated the incompressible flow in a constant area rectangular S-duct mounted in a wind tunnel. The ducts had two 35° bends, and tests were conducted to a 30° angle of attack and to a 10° angle of yaw. The Reynolds number, based on diameter, varied between 2.1×10^5 and 2.7×10^5. Total-pressure contours, recovery, and turbulence levels were reported. Flow separation, large exit flow distortion, a pair of counterrotating vortices, and high turbulence levels were observed. McMillan (ref. 16) tested a diffusing duct of 40° to obtain incompressible computational fluid dynamics (CFD) validation data. A pair of counterrotating streamwise vortices dominated the flow. Schmidt et al. (ref. 17) conducted experiments to provide incompressible CFD validation data for a rectangular, constant area duct with S-ducts upstream and downstream. The Reynolds numbers tested were 790 and 40 000, based on hydraulic diameter. A second duct was tested with a circular cross section and a 45°–45° uniform area S-duct upstream and a 22.5°–22.5° downstream S-duct diffuser.

Numerical Analyses

Rowe (ref. 18) performed early experiments and inviscid computations of flow in a 45°–45° S-bend and a 180° pipe with a Reynolds number of 2.36×10^5. He solved the continuity equation in the crossplane for the secondary flow and solved a Poisson equation with the vorticity source term to determine the secondary-flow velocities. Towne and Anderson (ref. 19) conducted a numerical study with a PNS computer program of a circular S-duct. The incompressible flow Reynolds number was 2000, based on diameter. They also analyzed the F-16 inlet duct with an elliptical inlet shape and round exit and with an area ratio of 1.3. A turbulent flow calculation was completed with $Re = 1.44\times10^7$ and an entrance Mach number of 0.9; the inlet flow field was specified. Good agreement with exit total-pressure data was obtained. Vakili et al. (refs. 20 and 21) reported experimental and computational results for a 30°–30° nondiffusing S-duct. The inlet Mach number was 0.6, the Reynolds number was 3.25×10^6 per foot, and the inlet boundary layer was 0.078 of the duct radius. The PNS computation agreed well with the experimental total pressures and velocity vectors. Towne (ref. 22) used a PNS code to predict the total-pressure field for several RAE inlet ducts with offsets of 0.3 and 0.45, with and without centerbody hubs. Calculated total-pressure profiles were in good agreement with experiment results.

Malechi and Lord (ref. 13) used a PNS code to calculate the flow field of two circular to rectangular transition ducts. These ducts produced a pair of counterrotating vortices like those of S-ducts. The authors concluded it was important to have available and accurate inlet boundary-layer profiles in order to accurately calculate the (fixed) input static-pressure field necessary for the PNS solution. The PNS solver underpredicted the vortex strength and the cross-sectional velocities. The *k-e* turbulence model was used, and they concluded that the turbulent eddy viscosity was (numerically) suppressed in the vortex core. Cosner (ref. 23) reported an FNS simulation of a compact, highly offset diffuser with an inlet Mach number of 0.777. The boundary layer separated from the inner bend of the diffuser at half the diffuser length. Predictions were also made for a different diffuser with an assumed uniform inflow (with a boundary layer) at Mach number 0.65. Static-pressure and boundary-layer profiles were not presented, nor were grid and turbulence model details.

Monson et al. (ref. 24 and personal communication with authors of ref. 24) compared experimental data and FNS numerical results for a rectangular (Space Shuttle Main Engine) 180° U-duct. The Mach number was 0.1, and the Reynolds numbers, based on channel height, were 10^5 and 10^6. They concluded that simple mixing length models are inadequate for strong secondary flows.

Conclusions From the Literature

Vortex pairs are evident in the exit planes of S-ducts, transition ducts, and bending rectangular ducts. These vortices are due to secondary flows induced by pressure gradients. Benchmark CFD validation data exist for incompressible flow (see, e.g., McMillan and Schmidt et al. (refs. 16 and 17, respectively)) The Vakili data (refs. 20 and 21) are among the few sets of compressible CFD validation data available. Therefore, a need exists for additional experimental data for code validation with strong crossflow. A possible limitation of both algebraic and *k-e* turbulence modeling for strong secondary flows has been noted by several researchers.

The mechanism that produces the low total-pressure region at the exit is an inviscid rotational phenomenon, provided an inlet boundary layer is present. This obviously requires correct inlet boundary conditions. The previous

computational investigations appear to be limited to FNS or PNS computations that did not account for the upstream effect of mass flow adjustment, boundary-layer growth, and flow blockage; that is, the published solutions have specified inlet conditions. The PNS solutions usually rely on an input inviscid static-pressure field, which is generally from an Euler or potential analysis. (Most PNS solvers are single pass and do not iterate on pressure.) The interior static-pressure fields for these calculations have not been presented, thus it is difficult to assess the accuracy of the complete flow field solution, especially in terms of secondary flow or exit velocity.

References

1. Vakili, A.D., et al.: Compressible Flow in a Diffusing S-Duct with Flow Separation. Heat Transfer and Fluid Flow in Rotating Machinery, W.J. Yang, ed., Hemisphere Publishing, 1987, pp. 201-211.
2. Cooper, G.K.: The Parc Code: Theory and Usage. AEDC-TR-87-24, Oct. 1987. (Avail. NTIS, AD-B115169.)
3. Pulliam, T.H.; and Steger, J.L.: Implicit Finite-Difference Simulations of Three Dimensional Compressible Flow. AIAA J., vol. 18, no. 2, Feb. 1980, pp. 159-167.
4. Jameson, A.; Schmidt, W.; and Turkel, E.: Numerical Solutions of the Euler Equations by Finite Volume Methods Using Runge-Kutta Time-Stepping Schemes. AIAA Paper 81-1259, June 1981.
5. Pulliam, T.H.: Euler and Thin Layer Navier-Stokes Codes: ARC2D, ARC3D. Notes for Computational Fluid Dynamics User's Workshop, The University of Tennessee Space Institute, Tullahoma, TN, UTSI Pub. E02-4005-023-84, 1984, pp. 15.1-15.85.
6. Baldwin, B.S.; and Lomax, H.: Thin Layer Approximation and Algebraic Model for Separated Turbulent Flows. AIAA Paper 78-257, Jan. 1978.
7. Dorrell, E.W.; and McClure, M.D.: On 3D Ingrid: Interactive Three-Dimensional Grid Generation. AEDC-TR-87-40, Apr. 1988. (Avail. NTIS, AD-B121739L.)
8. Harloff, G.J., et al.: Three-Dimensional Compressible, Turbulent Computations in a Non-Diffusing S-Duct. NASA CR-185228, 1990.
9. Bansod, P.; and Bradshaw, P.: The Flow in S-Shaped Ducts. Aeronaut. Q., vol. 23, May 1972, pp. 131-140.
10. Crawford, M.E.; and Kays, W.M.: STAN5: A Program for Numerical Computation of Two-Dimensional, Internal and External Boundary Layer Flows. NASA CR-2742, 1976.
11. van den Berg, B.: A European Collaborative Investigation of the Three-Dimensional Turbulent Shear Layers of a Swept Wing. Fluid Dynamics of Three-Dimensional Turbulent Shear Flows and Transition. AGARD-CP-438, AGARD, Neuilly-Sur-Seine, France, 1989, pp. 25-1 to 25-19.
12. Squire, H.B.; and Winter, K.G.: The Secondary Flow in a Cascade of Airfoils in a Nonuniform Stream. J. Aeronaut. Sci., vol. 18, no. 4, Apr. 1951, pp. 271-277.
13. Malecki, R.E.; and Lord, W.K.: Parabolized Navier-Stokes Analysis of Circular-to-Rectangular Transition Duct Flows. SAE Paper 88-1480, Oct. 1988.
14. Willmer, A.C.; Brown, T.W.; and Goldsmith, E.L.: Effects of Intake Geometry on Circular Pitot Intake Performance at Zero and Low Forward Speeds. Aerodynamics of Power Plant Installations, AGARD CP-301, AGARD, Neuilly-Sur-Seine, France, May 1981, pp. 5-1 to 5-16.
15. Guo, R.W.; and Seddon, J.: An Investigation of the Swirl in an S-Duct. Aeronaut. Q., vol. 33, Feb. 1982, pp. 25-58.
16. McMillan, O.J.: Mean-Flow Measurements of the Flow Field in a Diffusing Bend. NASA CR-3634, 1982.
17. Schmidt, M.C.; Whitelaw, J.H.; and Yianneskis, M.: Flow in Out-of-Plane Double S-Bends. 6th Symposium on Turbulent Shear Flows, Pennsylvania State University, 1988, pp. 13-3-1 to 13-3-6.
18. Rowe, M.: Measurements and Computations of Flow in Pipe Bends. J. Fluid Mech., vol. 43, pt. 4, Oct. 2, 1970, pp. 771-783.
19. Towne, C.E.; and Anderson, B.H.: Numerical Simulation of Flows in Curved Diffusers With Cross-Sectional Transitioning Using a Three-Dimensional Viscous Analysis. AIAA Paper 81-0003, Jan. 1981. (Also, NASA TM-81672.)
20. Vakili, A.D., et al.: Comparison of Experimental and Computational Compressible Flow in an S-Duct. AIAA Paper 84-0033, Jan. 1984.
21. Vakili, A.D., et al.: Measurement of Compressible Secondary Flow in a Circular S-Duct. AIAA Paper 83-1739, July 1983.
22. Towne, C.E.; and Flitcroft, J.E.: Analysis of Intake Ducts Using a Three-Dimensional Viscous Marching Procedure. Presented at the First World Congress on Computational Mechanics, Austin, TX, Sept. 1986.
23. Cosner, R.R.: Transonic Propulsion System Integration Analysis at McDonnell Aircraft Company. Transonic Symposium: Theory, Application, and Experiment, J.T. Foughner, Jr., ed., NASA CP-3020, Vol. 1, Pt. 2, 1988, pp. 409-436.
24. Monson, D.J.; Seegmiller, H.L.; and McConnaughey, P.K.: Comparison of LDV Measurements and Navier-Stokes Solutions in a Two-Dimensional 180-Degree Turn-Around Duct. AIAA Paper 89-0275, Jan. 1989.

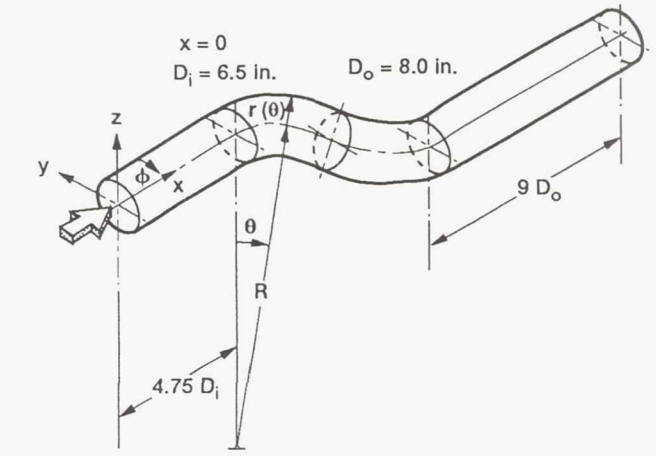

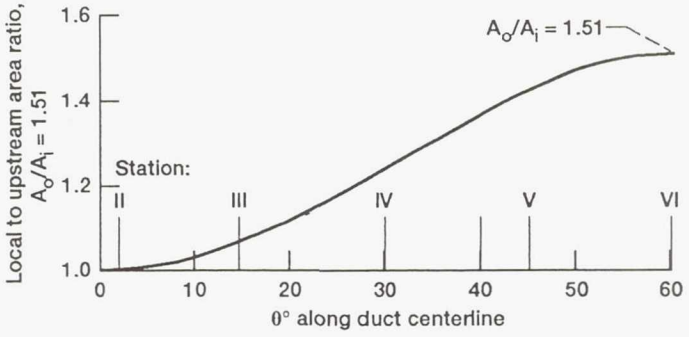

(a) Dimensions and coordinates.

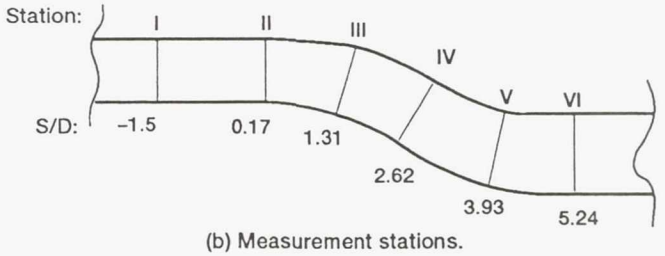

(b) Measurement stations.

Figure 1.—Coordinates and geometry of diffusing S-duct. Mean radius of bends, R, 32.5 in.

(a) Plane of symmetry.

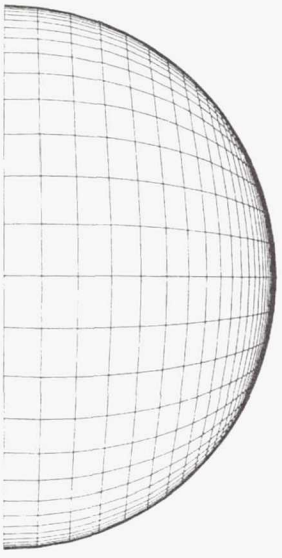

(b) Cross-sectional view.

Figure 2.—H-grid.

(a) Plane of symmetry.

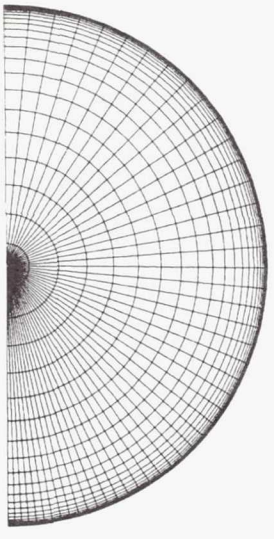

(b) Cross-sectional view.

Figure 3.—O-grid.

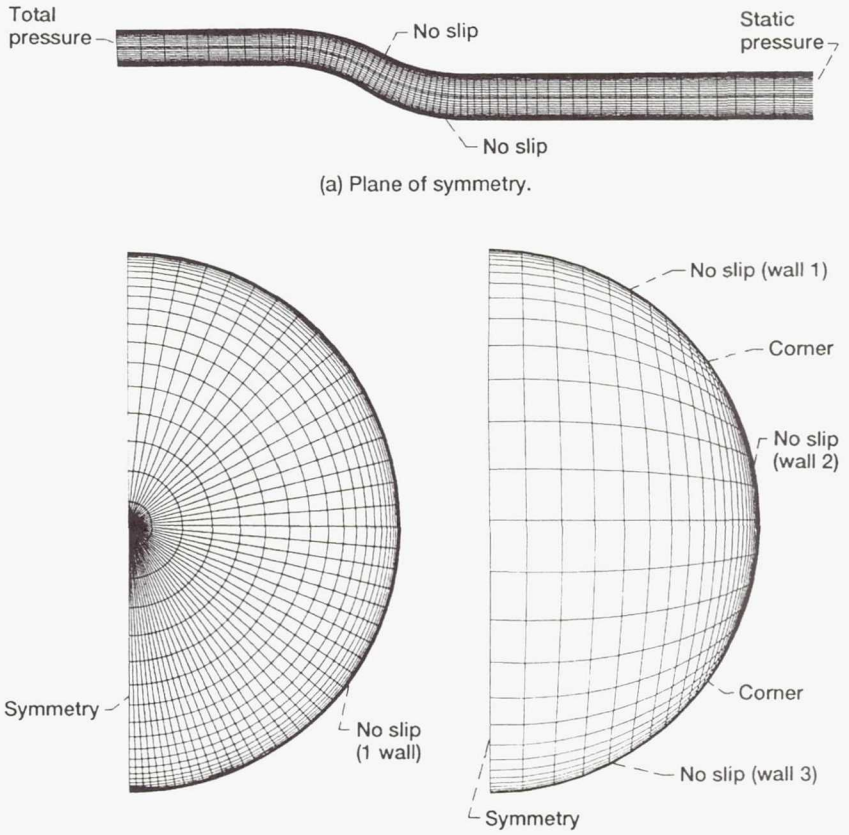

(a) Plane of symmetry.

(b) Cross-section of O-grid.

(c) Cross section of H-grid.

Figure 4.—Boundary conditions.

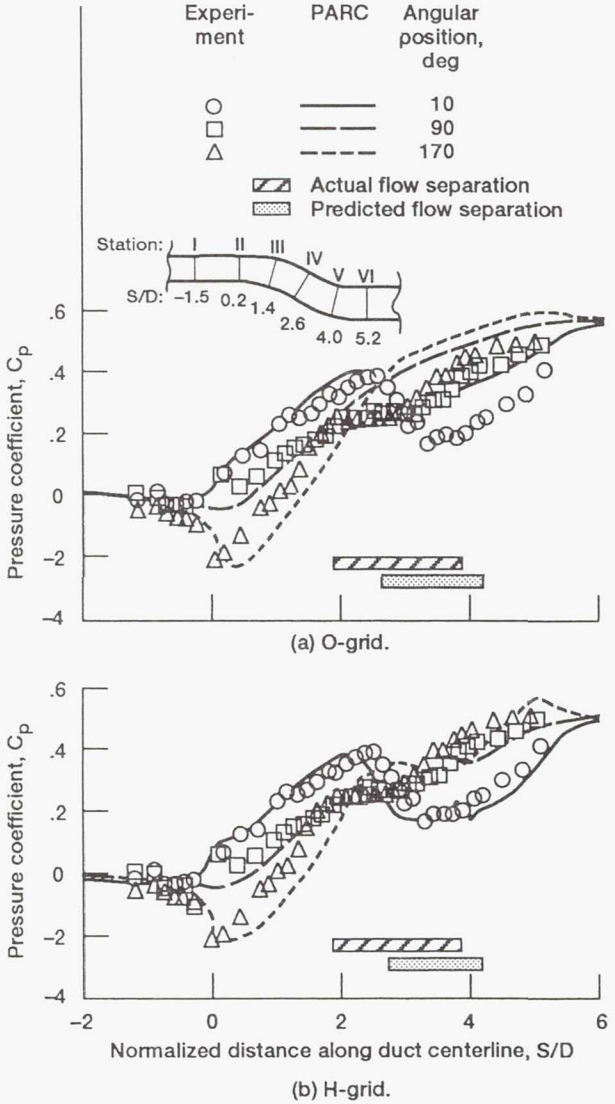

Figure 5.—Surface static pressure distributions.

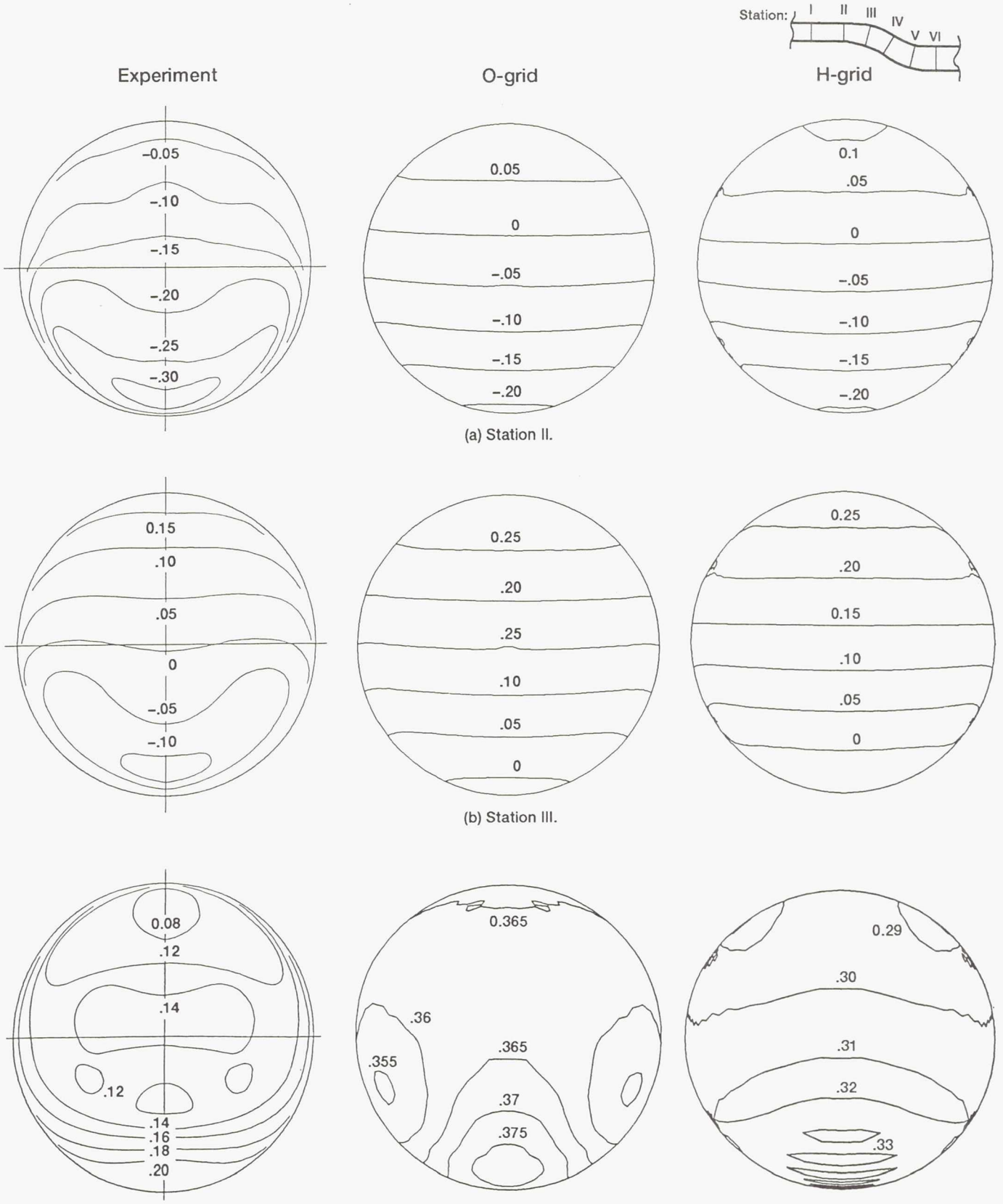

(a) Station II.

(b) Station III.

(c) Station IV.

Figure 6.—Static pressure coefficients.

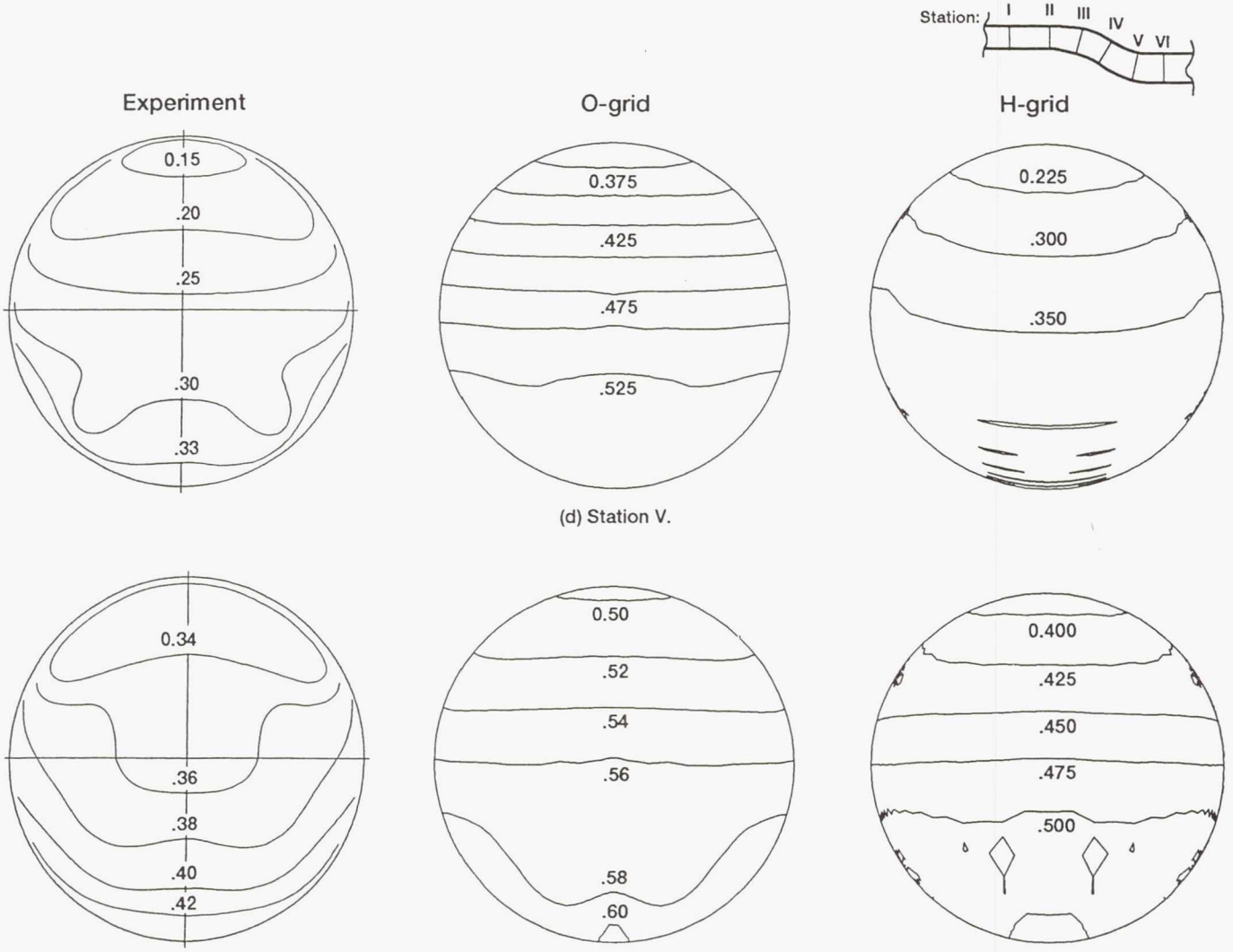

(d) Station V.

(e) Station VI.

Figure 6.—Concluded.

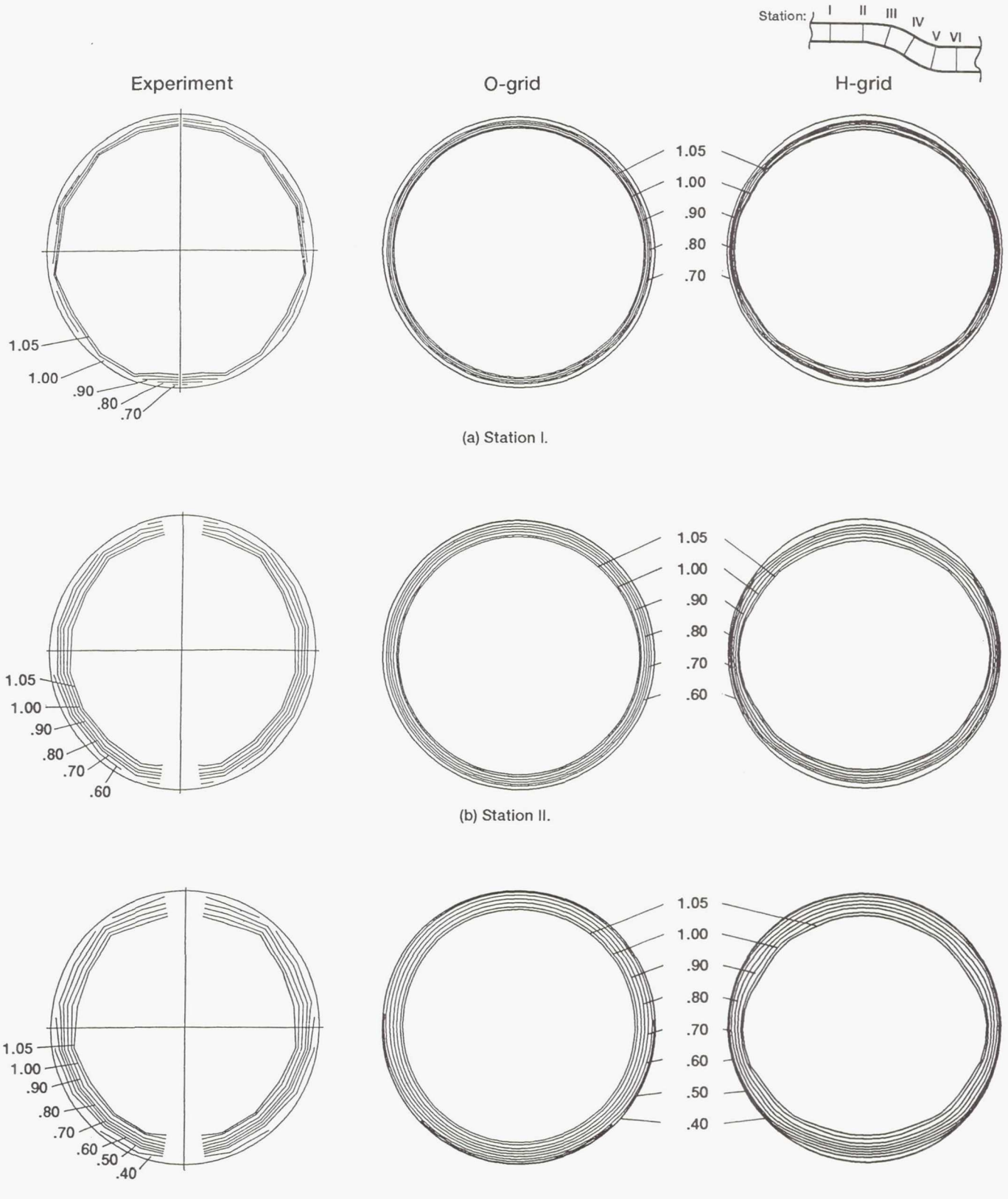

(a) Station I.

(b) Station II.

(c) Station III.

Figure 7.—Total pressure coefficients.

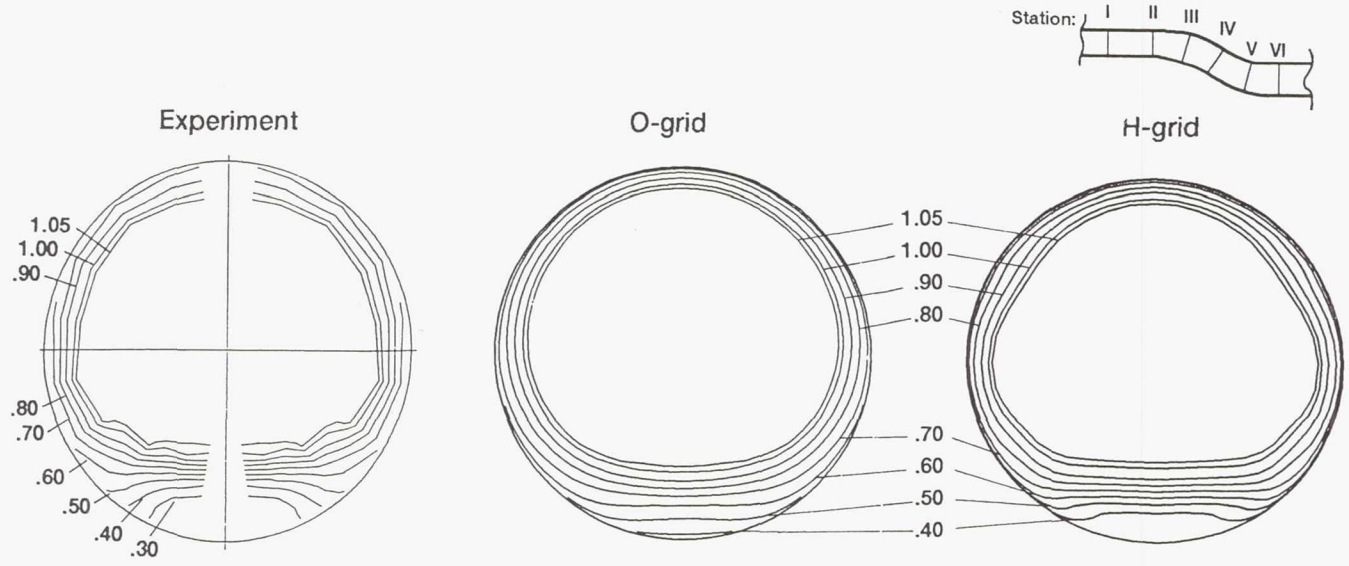

(d) Station IV.

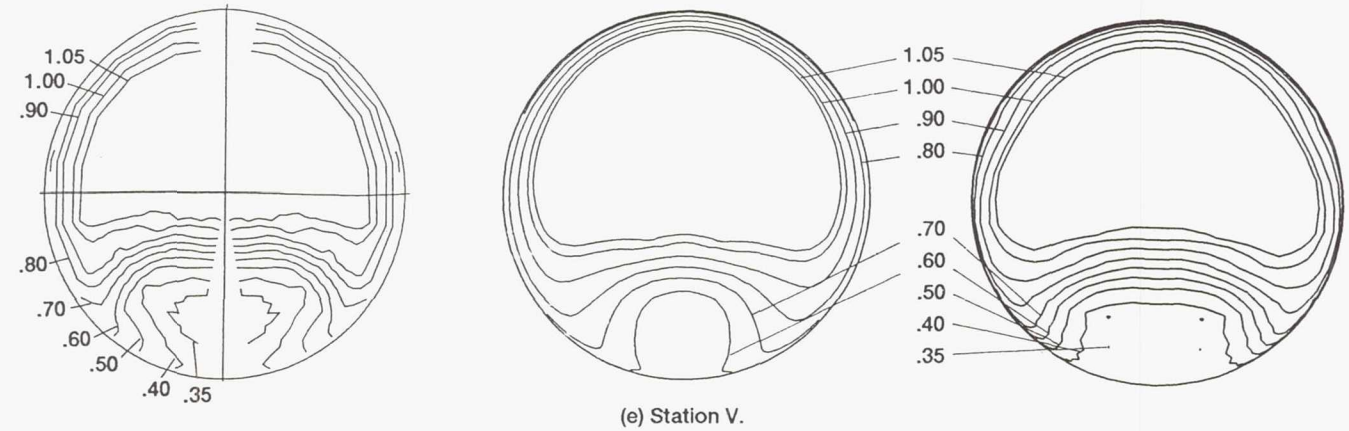

(e) Station V.

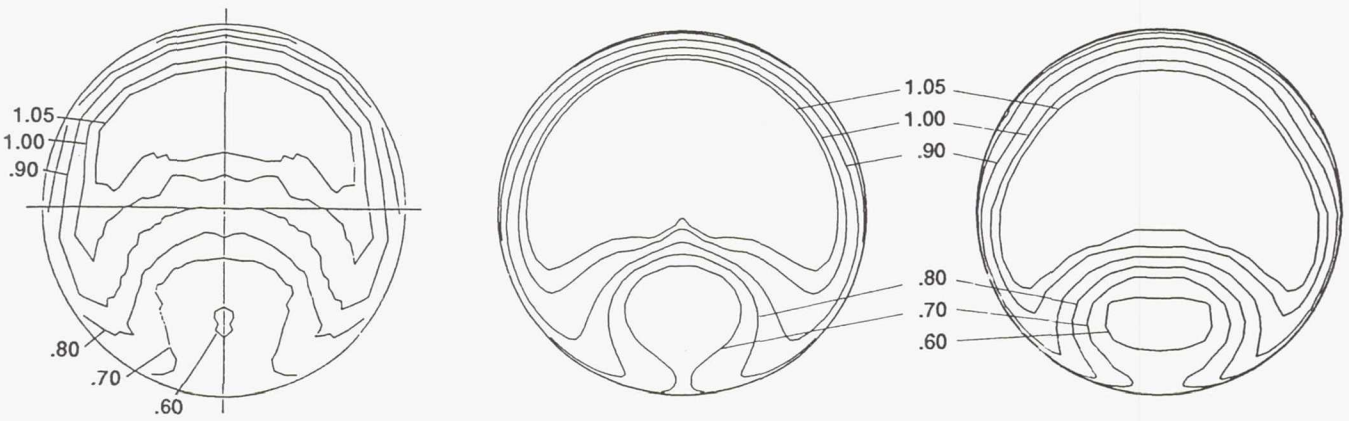

(f) Station VI.

Figure 7.—Concluded.

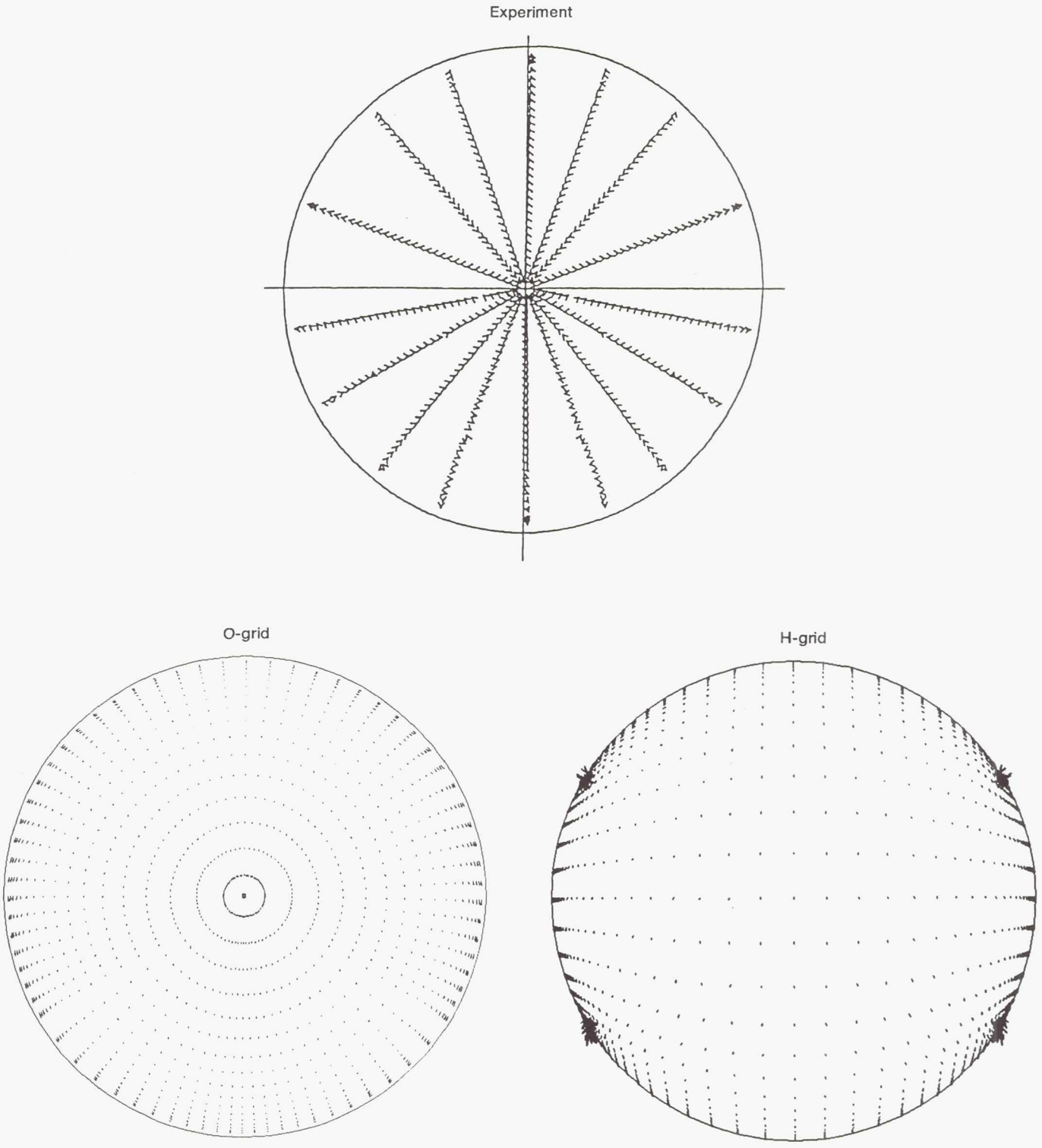

(a) Station I.

Figure 8.—Velocity vectors.

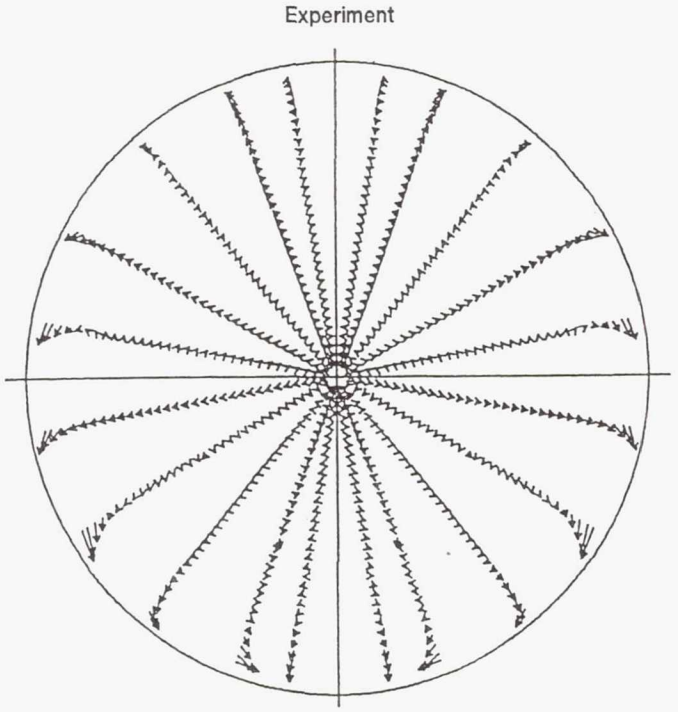

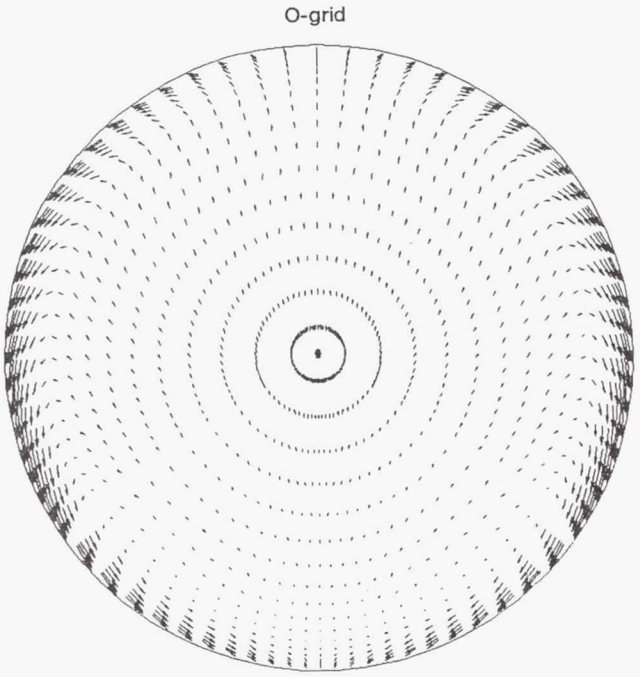

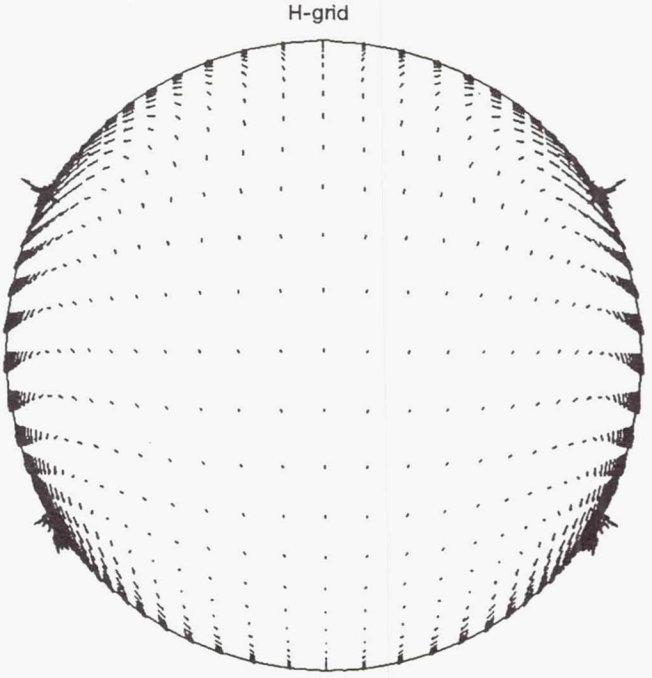

(b) Station III.

Figure 8.—Continued.

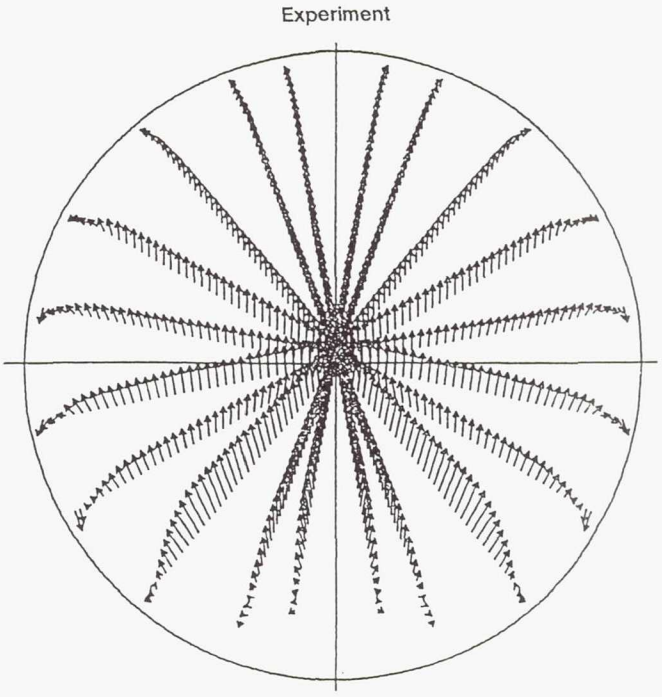

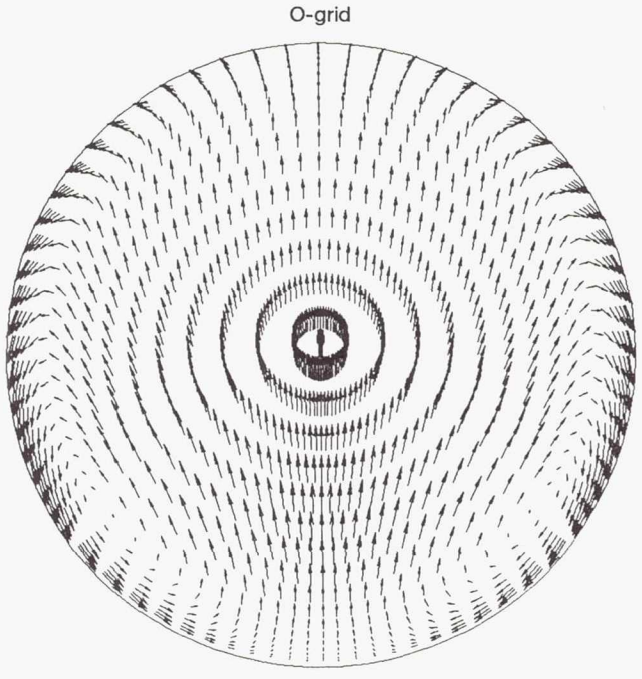

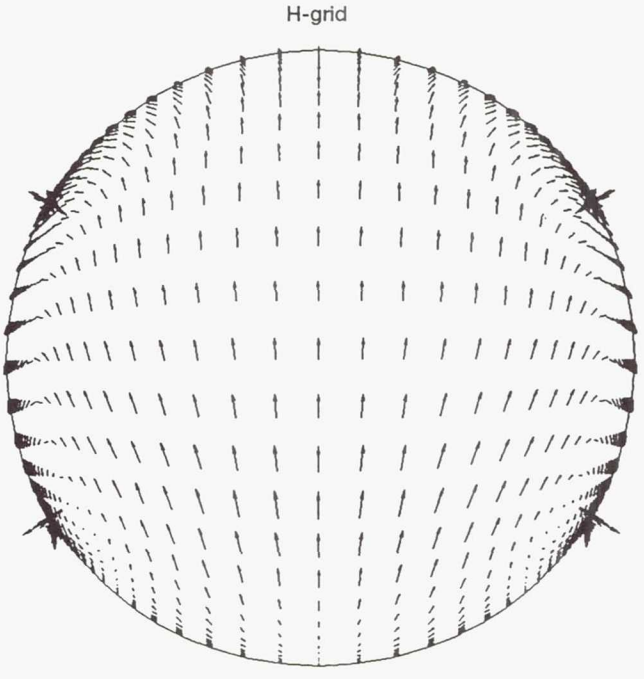

(c) Station IV.

Figure 8.—Continued.

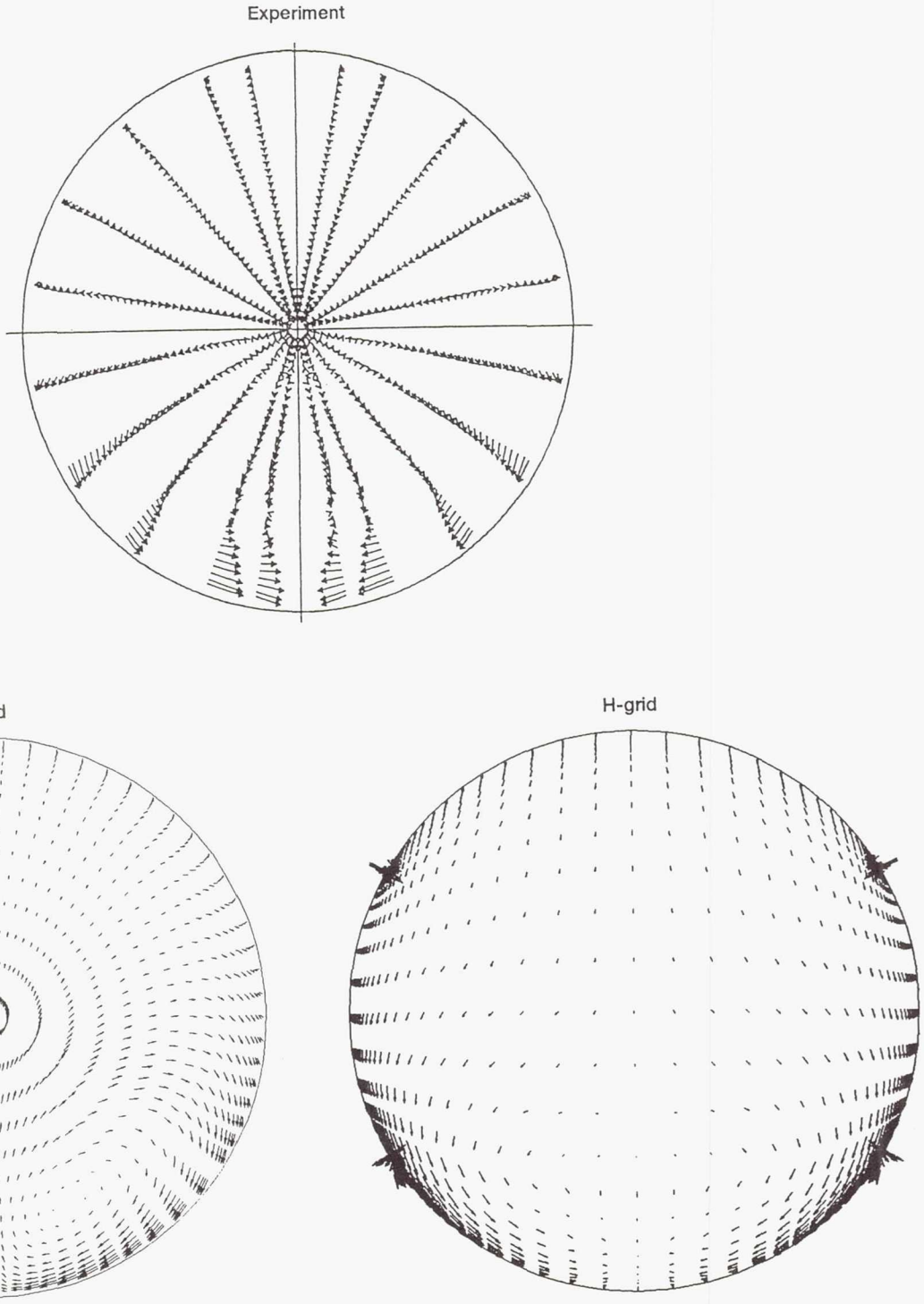

(d) Station V.

Figure 8.—Continued.

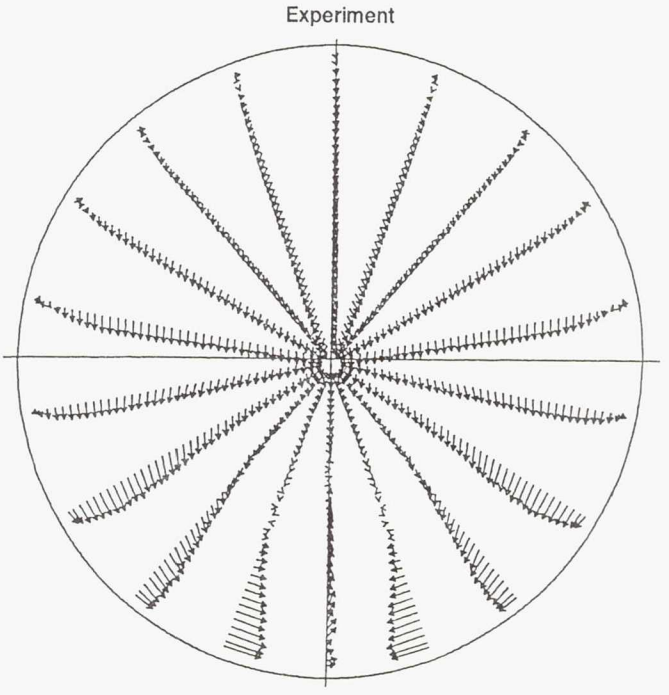

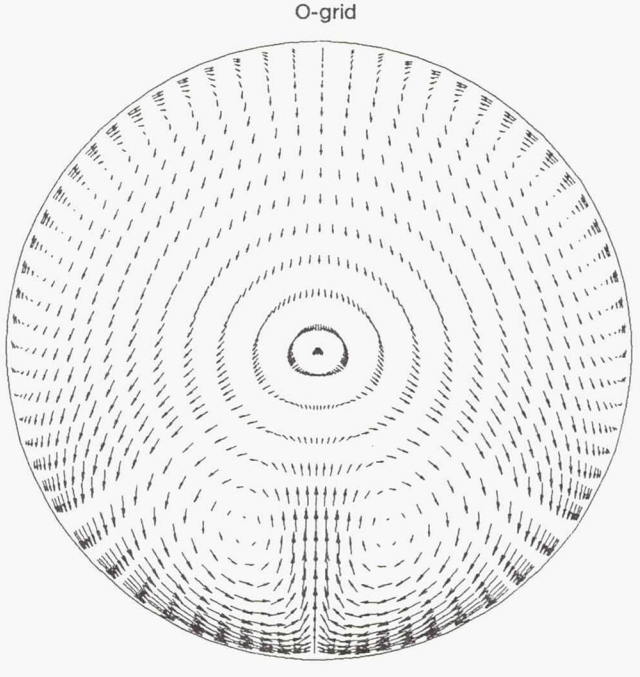

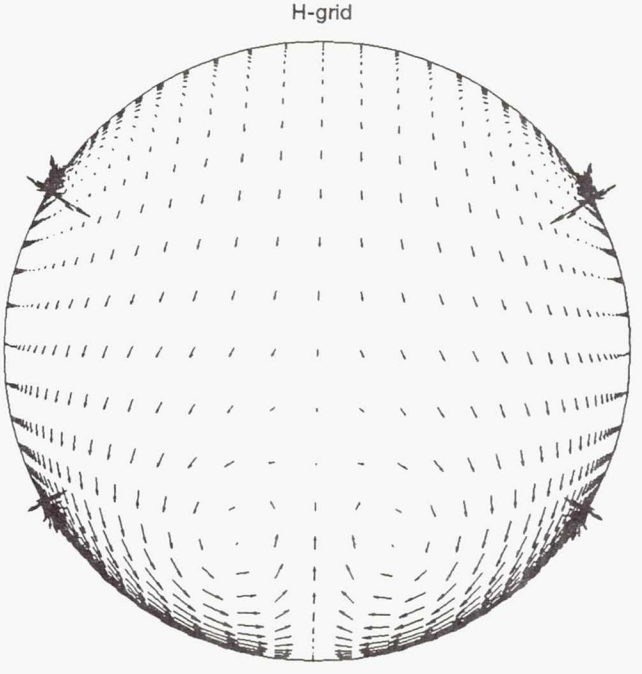

(e) Station VI.

Figure 8.—Concluded.

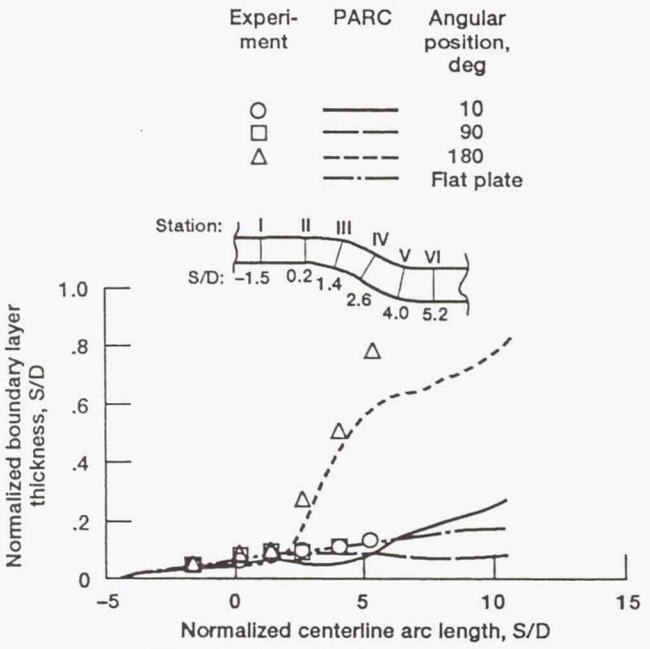

Figure 9.—Boundary layer growth.

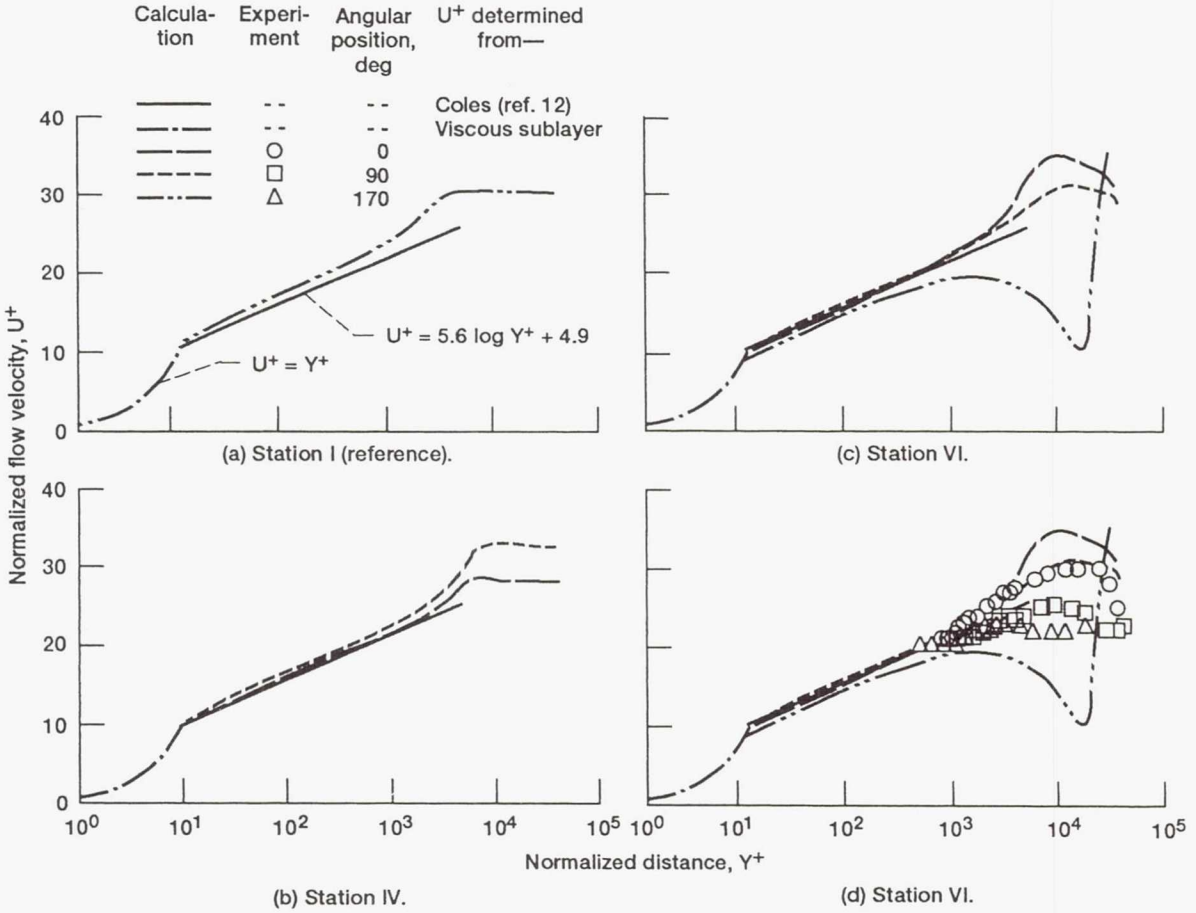

(a) Station I (reference).

(c) Station VI.

(b) Station IV.

(d) Station VI.

Figure 10.—Velocity profiles.

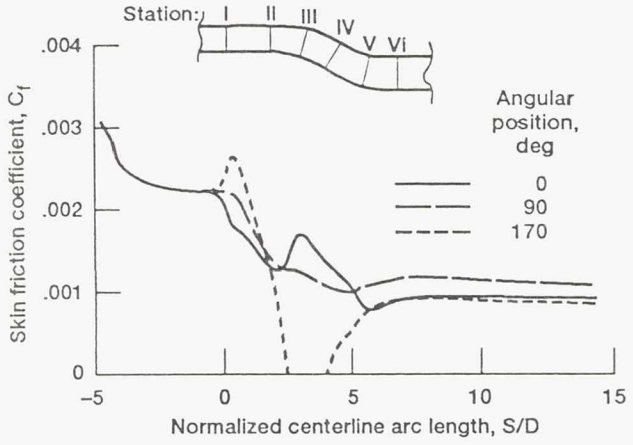

Figure 11.—Skin friction as function of arc length.

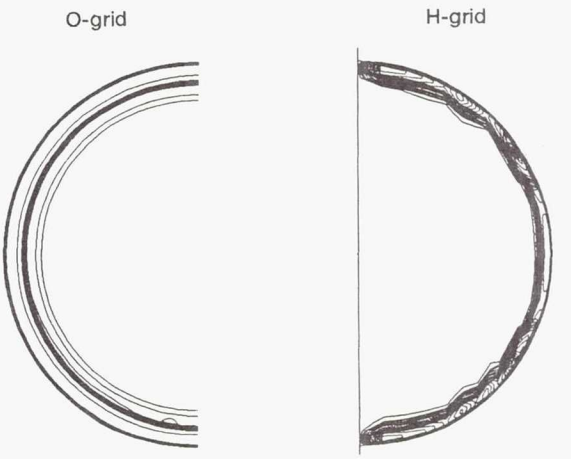

(a) Station I.

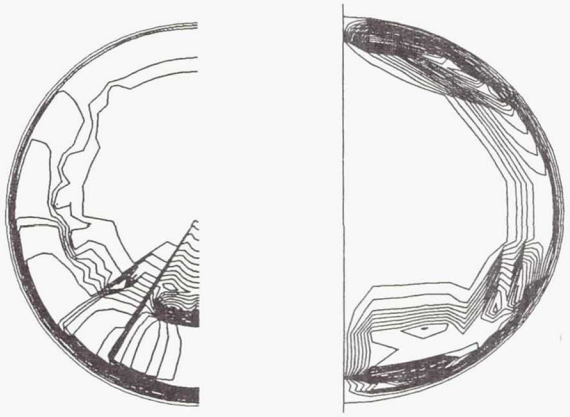

(b) Station IV.

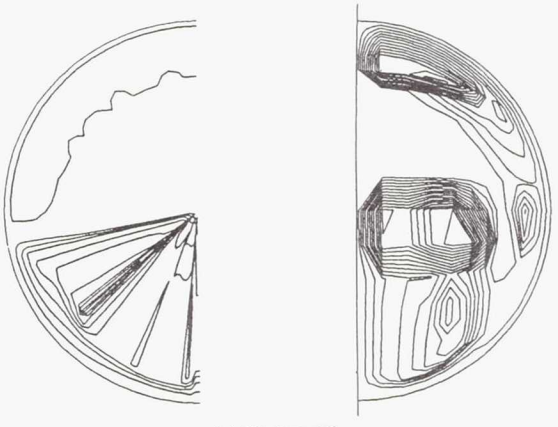

(c) Station VI.

Figure 12.—Turbulent viscosity contours.

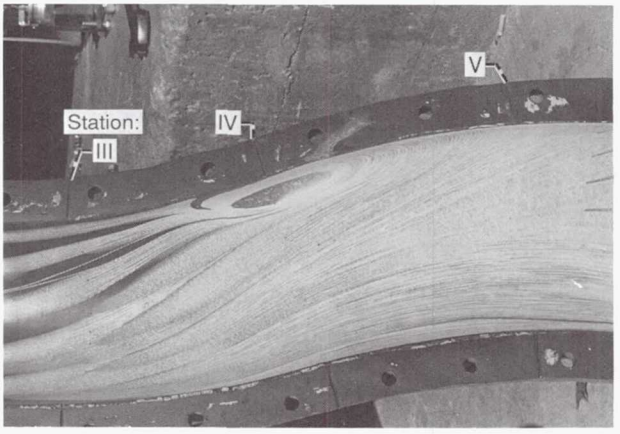

(a) Experiment.

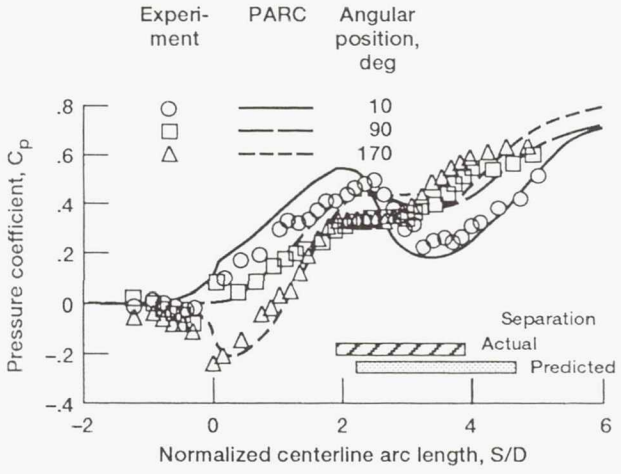

Figure 13.—Surface static pressure distributions.

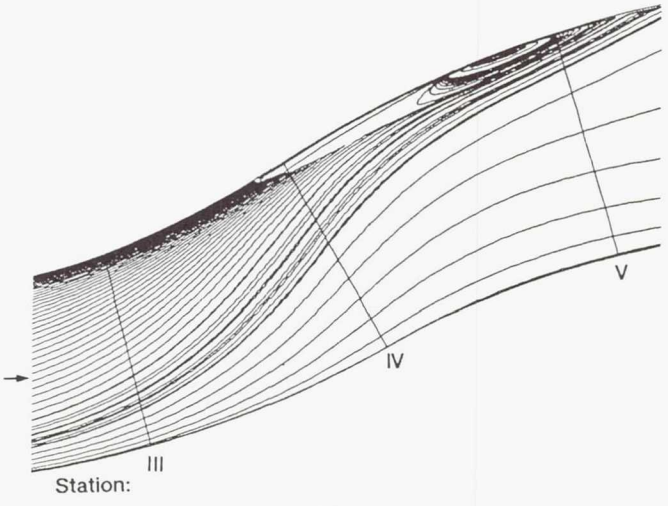

(b) O-grid.

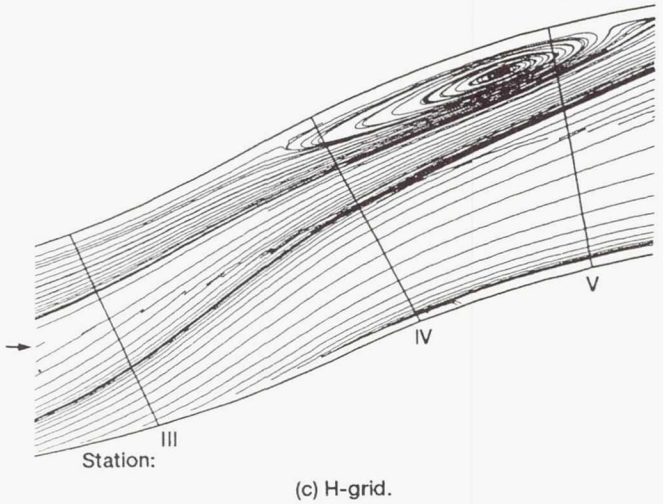

(c) H-grid.

Figure 14.—Flow separation.

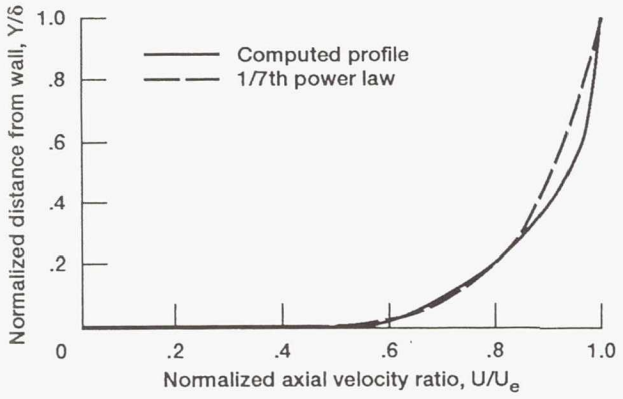

Figure 15.—Upstream velocity profile at station I.

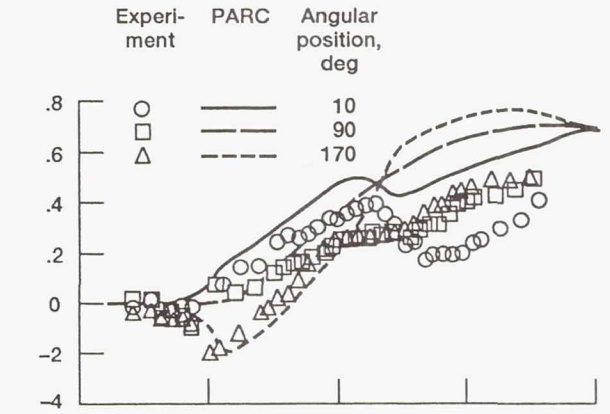

(a) Irrotational flow.

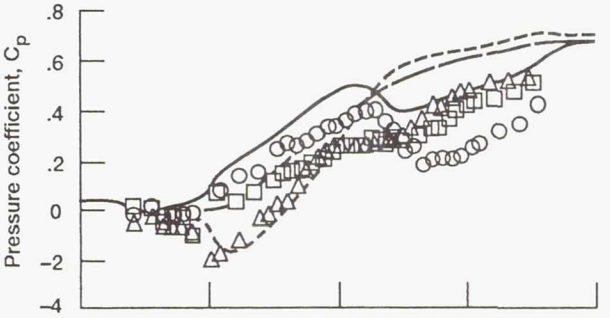

(b) Invisced, rotational flow.

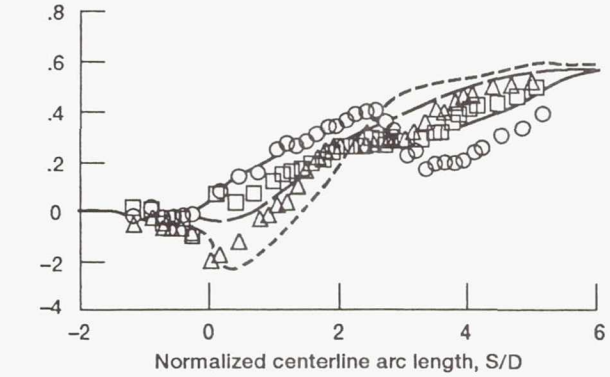

(c) Turbulent flow.

Figure 16.—Surface static pressure distributions.

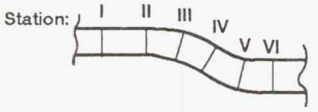

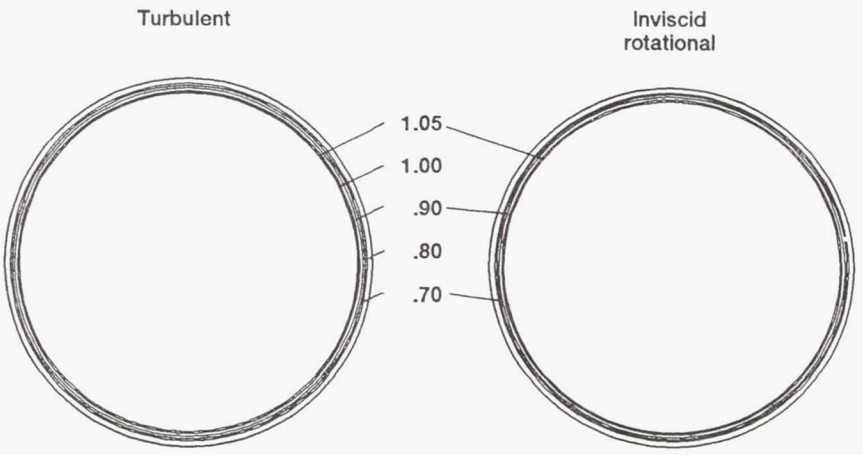

(a) Station I.

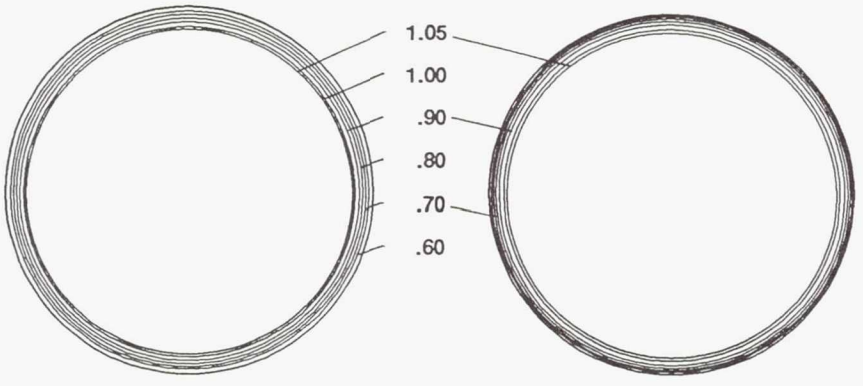

(b) Station II.

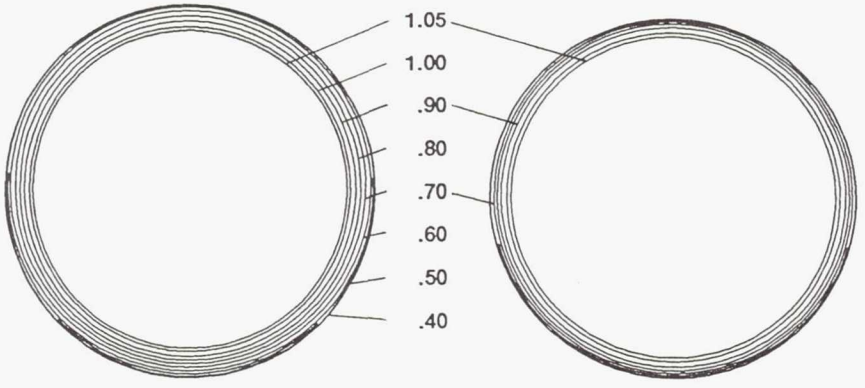

(c) Station III.

Figure 17.—Total pressure coefficients for turbulent flow and inviscid, rotational flow.

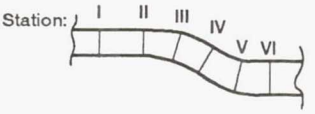

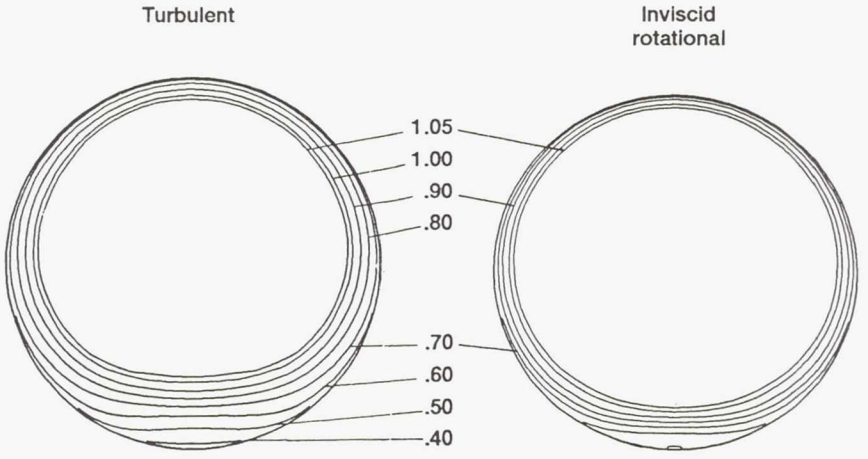

(d) Station IV.

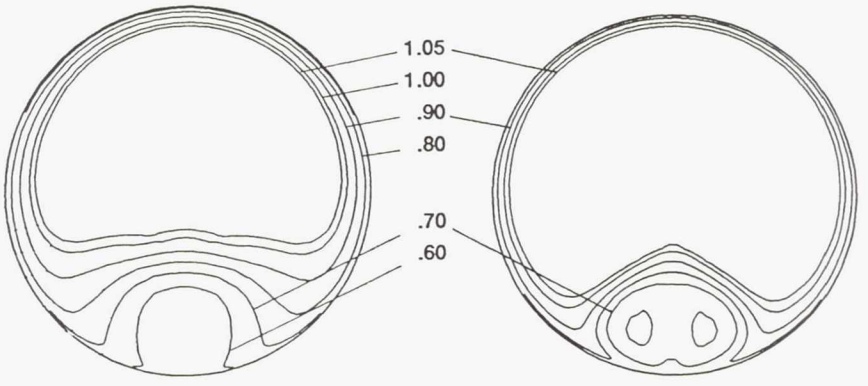

(e) Station V.

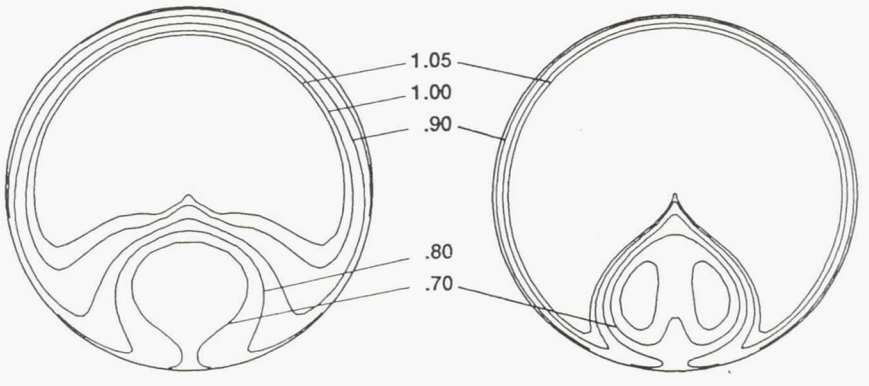

(f) Station VI.

Figure 17.—Concluded.

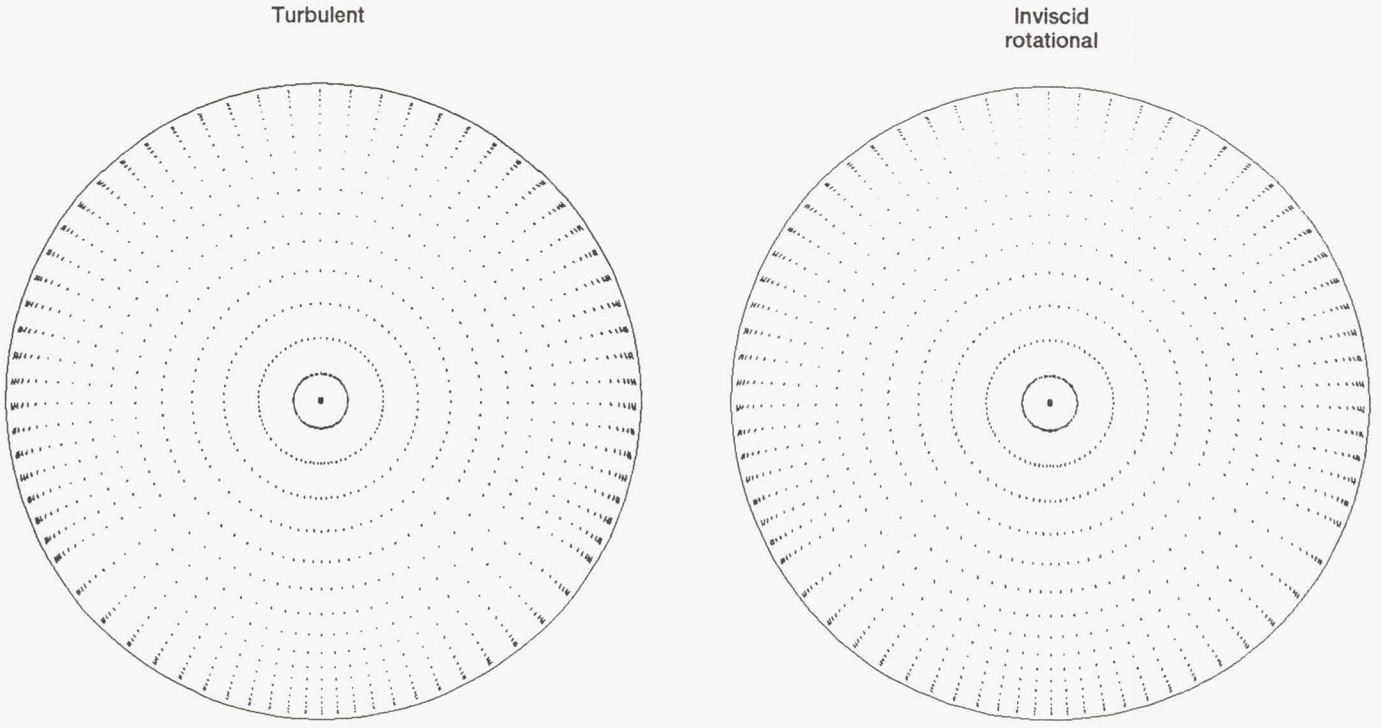

(a) Station II.

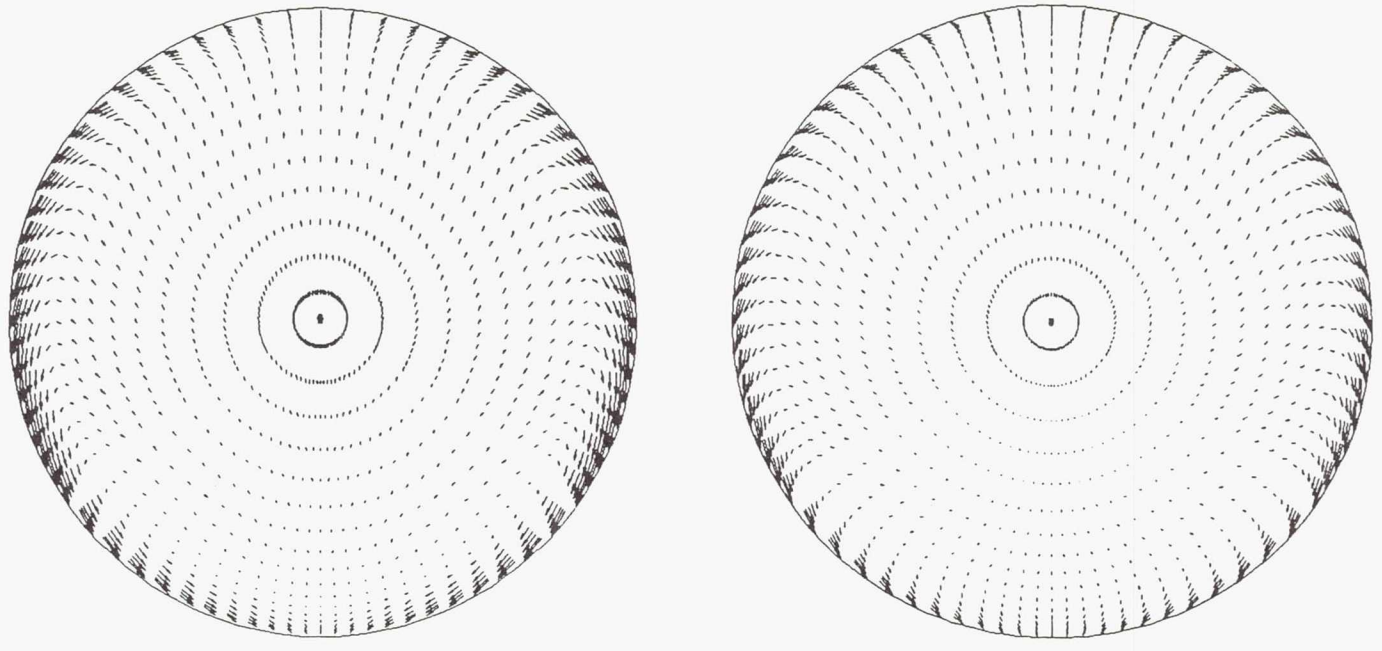

(b) Station III.

Figure 18.—Velocity vectors for turbulent flow and inviscid, rotational flow.

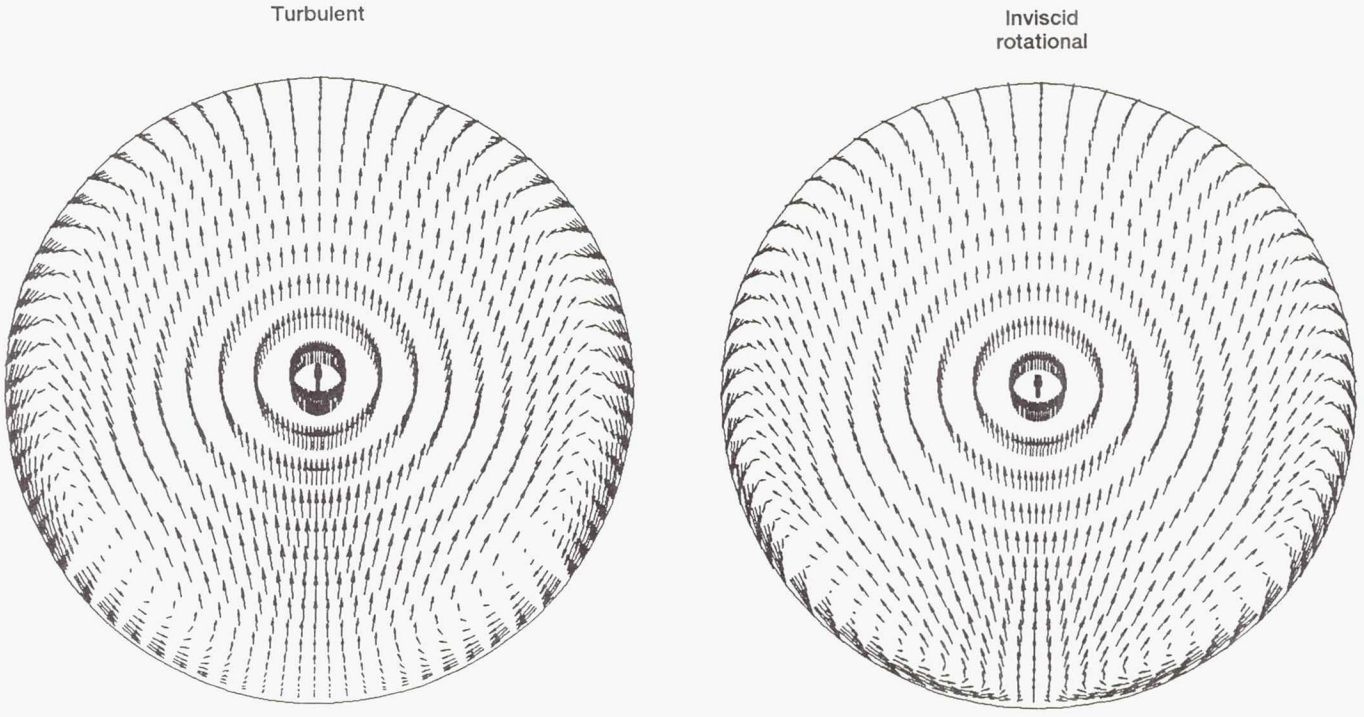

(c) Station IV.

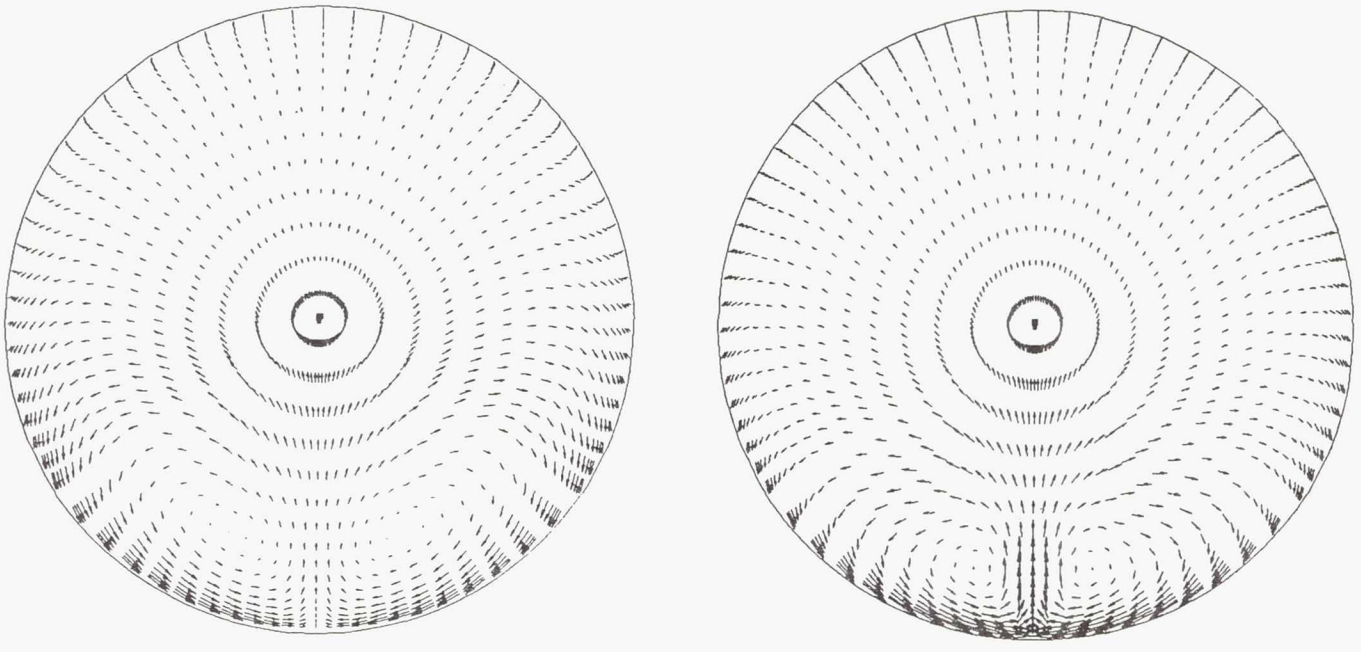

(d) Station V.

Figure 18.—Continued.

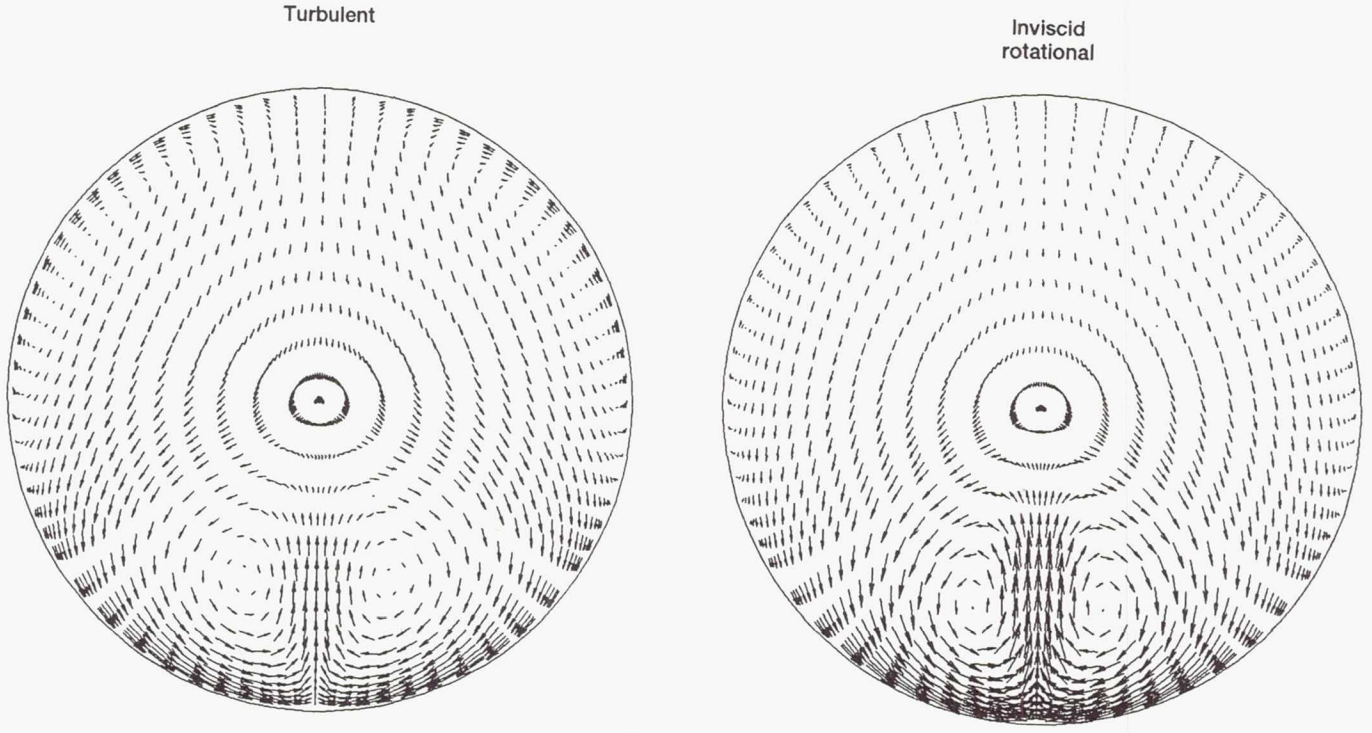

(e) Station VI.

Figure 18.—Concluded.

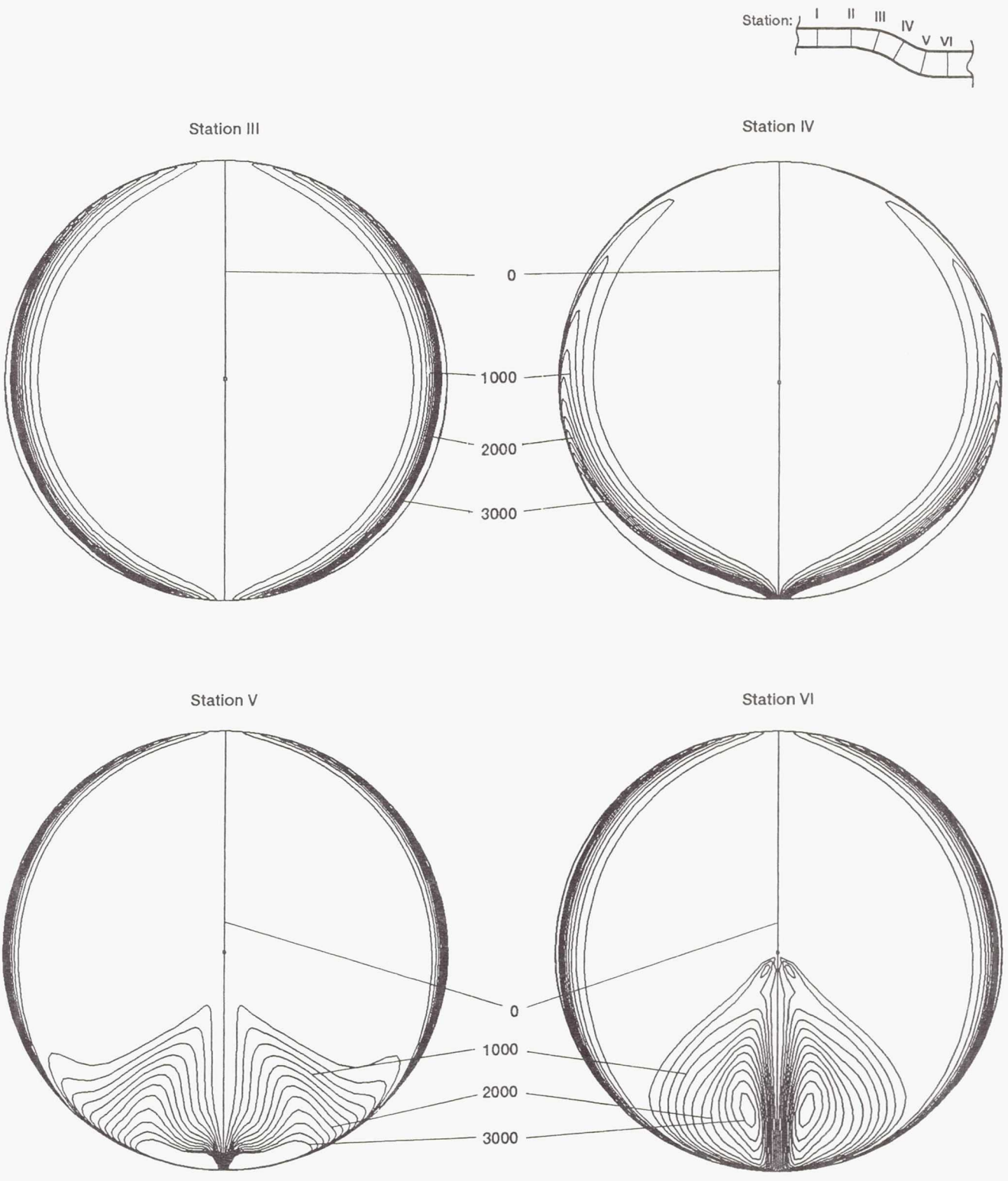

(a) Inviscid-rotational case.

Figure 19.—Streamwise vorticity contours. Note: contour levels are the same in parts (a) and (b). Units are per second.

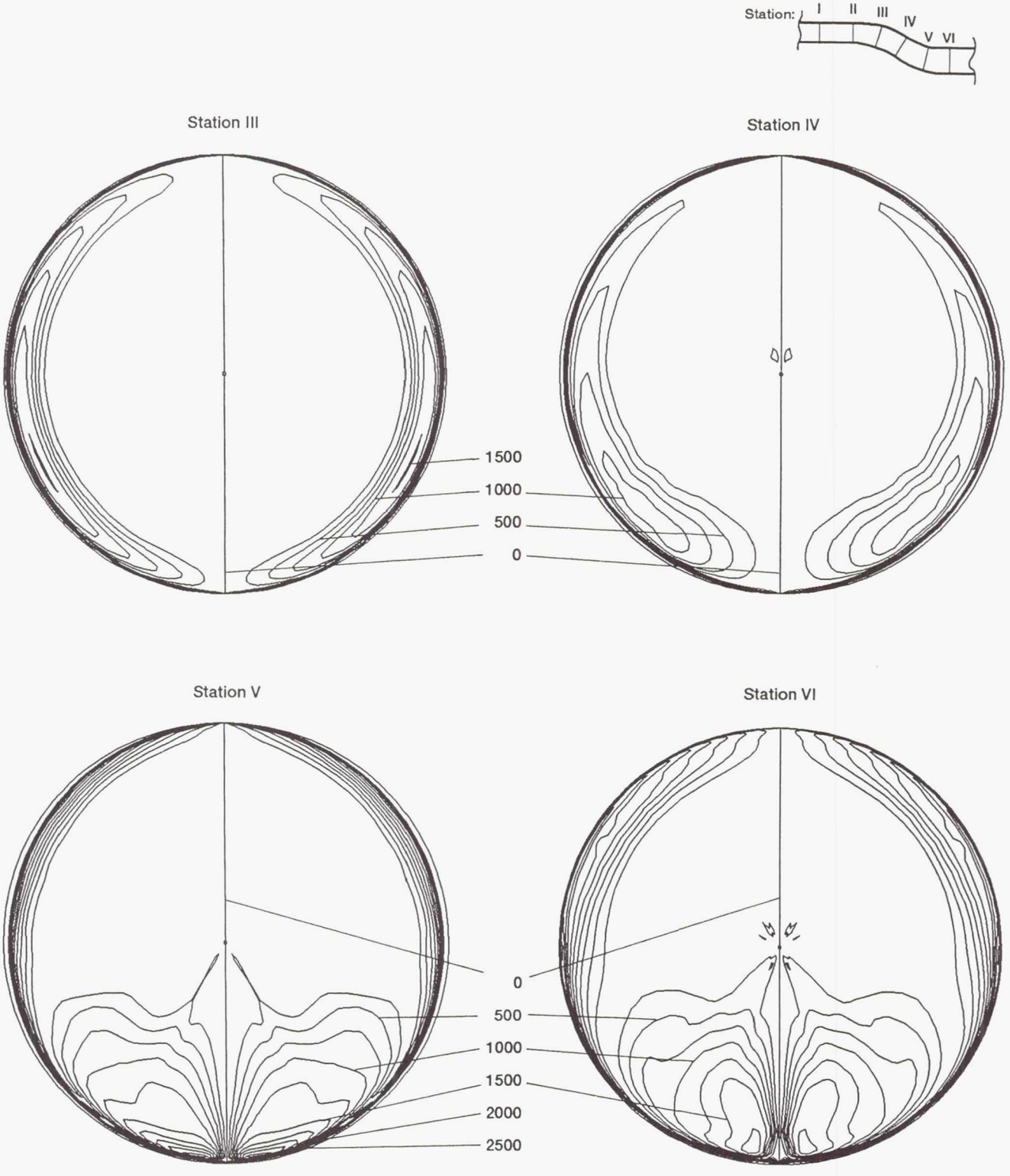

(b) Fully turbulent case.

Figure 19.—Concluded.

REPORT DOCUMENTATION PAGE

Form Approved
OMB No. 0704-0188

1. AGENCY USE ONLY (*Leave blank*)	2. REPORT DATE	3. REPORT TYPE AND DATES COVERED
	April 1992	Final Contractor Report

4. TITLE AND SUBTITLE

Three-Dimensional Compressible Turbulent Computations for a Diffusing S-Duct

5. FUNDING NUMBERS

WU–533–02–30
NAS3–25266

6. AUTHOR(S)

C.F. Smith, J.E. Bruns, G.J. Harloff, and J.R. DeBonis

7. PERFORMING ORGANIZATION NAME(S) AND ADDRESS(ES)

Sverdrup Technology, Inc.
Lewis Research Center Group
2001 Aerospace Parkway
Brook Park, Ohio 44142

8. PERFORMING ORGANIZATION REPORT NUMBER

E–6172

9. SPONSORING/MONITORING AGENCY NAMES(S) AND ADDRESS(ES)

National Aeronautics and Space Administration
Lewis Research Center
Cleveland, Ohio 44135–3191

10. SPONSORING/MONITORING AGENCY REPORT NUMBER

NASA CR–4392

11. SUPPLEMENTARY NOTES

Project Manager, Robert E. Coltrin, Propulsion Systems Division, NASA Lewis Research Center. Responsible person, C.F. Smith, (216) 826–6708.

12a. DISTRIBUTION/AVAILABILITY STATEMENT

Unclassified - Unlimited
Subject Category 02

12b. DISTRIBUTION CODE

13. ABSTRACT ***(Maximum 200 words)***

The purpose of the present study was to evaluate the capability of the computational fluid dynamics computer program PARC3D to model flow in a typical diffusing subsonic S-duct, with strong secondary flows. This evaluation is needed to provide confidence in the analysis of aircraft inlets, which have similar geometries. The performance predictions include total-pressure profiles, static pressures, velocity profiles, boundary-layer data, and skin friction data. Flow in the S-duct is subsonic, and the boundary layers are assumed to be turbulent. The results, for both H- and O-grid solutions, are compared with existing test data.

14. SUBJECT TERMS

Computational fluid dynamics, Ducts; Ducted flow; Turbulent flow

15. NUMBER OF PAGES

16. PRICE CODE

17. SECURITY CLASSIFICATION OF REPORT	18. SECURITY CLASSIFICATION OF THIS PAGE	19. SECURITY CLASSIFICATION OF ABSTRACT	20. LIMITATION OF ABSTRACT
Unclassified	Unclassified	Unclassified	

NSN 7540-01-280-5500

Standard Form 298 (Rev. 2-89)
Prescribed by ANSI Std. Z39-18
298-102

NASA-Langley, 1992